Featured Article

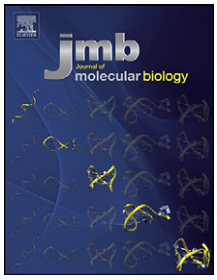

# Folding and Unfolding Pathways of the Human Telomeric G-Quadruplex

**Robert D. Gray, John O. Trent and Jonathan B. Chaires**

***James Graham Brown Cancer Center,*** *University of Louisville, Louisville, KY 40202, USA*

***Correspondence to Jonathan B. Chaires:*** *505 South Hancock Street, Louisville, KY 40202, USA.*
*jchaires@louisville.edu*
http://dx.doi.org/10.1016/j.jmb.2014.01.009
***Edited by S. A. Woodson***

***Robert D. Gray, John O. Trent and Jonathan B. Chaires***

## Abstract

Sequence analogs of human telomeric DNA such as d[AGGG(TTAGGG)$_3$] (Tel22) fold into monomeric quadruplex structures in the presence of a suitable cation. To investigate the pathway for unimolecular quadruplex formation, we monitored the kinetics of $K^+$-induced folding of Tel22 by circular dichroism (CD), intrinsic 2-aminopurine fluorescence, and fluorescence resonance energy transfer (FRET). The results are consistent with a four-step pathway $U \leftrightarrow I_1 \leftrightarrow I_2 \leftrightarrow I_3 \leftrightarrow F$ where U and F represent unfolded and folded conformational ensembles and $I_1$, $I_2$, and $I_3$ are intermediates. Previous kinetic studies have shown that $I_1$ is formed in a rapid pre-equilibrium and may consist of an ensemble of "prefolded" hairpin structures brought about by cation-induced electrostatic collapse of the DNA. The current study shows that $I_1$ converts to $I_2$ with a relaxation time $\tau_1 = 0.1$ s at 25 °C in 25 mM KCl. The CD spectrum of $I_2$ is characteristic of an antiparallel quadruplex that could form as a result of intramolecular fold-over of the $I_1$ hairpins. $I_3$ is relatively slowly formed ($\tau_2 \approx 3700$ s) and has CD and FRET properties consistent with those expected of a triplex structure as previously observed in equilibrium melting studies. $I_3$ converts to F with $\tau_3 \approx 750$ s. Identical pathways with different kinetic constants involving a rapidly formed antiparallel intermediate were observed with oligonucleotides forming mixed parallel/antiparallel hybrid-1 and hybrid-2 topologies {e.g. d[TTGGG(TTAGGG)$_3$A] and d[TAGGG(TTAGGG)$_3$TT]}. Aspects of the kinetics of unfolding were also monitored by the spectroscopic methods listed above and by time-resolved fluorescence lifetime measurements using a complementary strand trap assay. These experiments reveal a slow, rate-limiting step along the unfolding pathway.


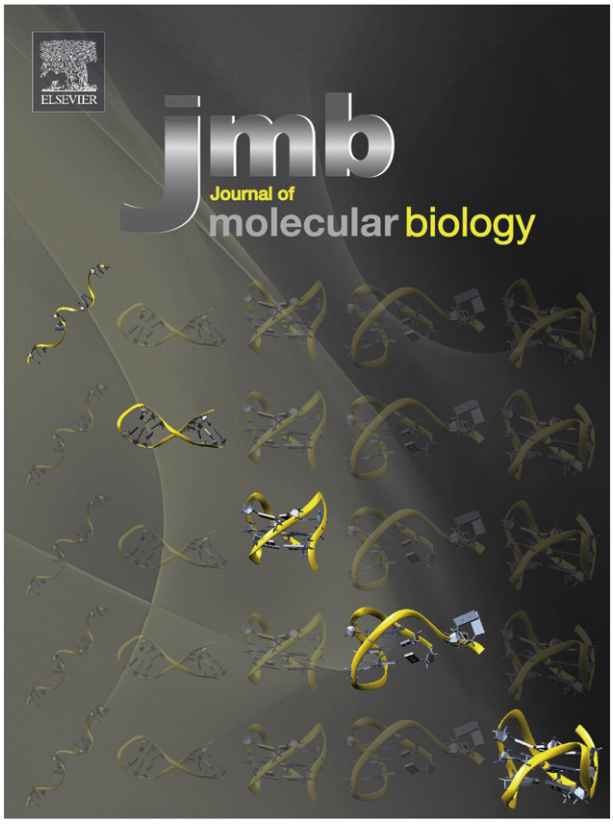


***Legend.*** *The cover shows DNA acting like proteins and RNA. The human telomere quadruplex folds into a compact structure that is topologically more complex than the canonical DNA duplex. The DNA folds from the single strand into the quadruplex by passing through multiple populated intermediate states, similar to pathways observed for protein and RNA folding.*

## Introduction

Understanding the mechanism by which biological macromolecules fold into their functional native conformations is a problem of fundamental interest and practical importance. Historically, since articulation of the "Leventhal paradox" [1], polypeptide and protein folding have been the primary focus of studies of macromolecular folding. Interest in protein folding has stimulated the development of methods and theory that have led to a general (but as yet incomplete) understanding of the steps involved in progressing from a disordered, unfolded polypeptide chain to an organized, compact folded structure. More recently, the kinetics of RNA folding into complex tertiary structures has attracted considerable interest, stimulated by the realization that these biopolymers (such as transfer RNAs, ribosomal RNA, and ribozymes) fold into compact structures with helical backbones and packed side chains analogous to globular proteins. Similarities and differences between protein and RNA folding mechanisms were noted [2]. The kinetics of folding of DNA has attracted comparatively less recent attention. Duplex DNA formation is perhaps regarded as somewhat boring because of the apparent simplicity and regularity of the canonical double helix, although classic kinetic studies of the association and unwinding of genomic DNA revealed slow, multiphasic kinetics arising from sequence complexity and rate-limiting nucleation events [3,4]. DNA kinetic studies have recently been largely focused on the folding of small duplex hairpins [5–11], model systems that, while fundamentally interesting, are unlikely to have much functional relevance. Recent advances show that certain DNA sequence elements in the genome can fold into noncanonical forms with complex tertiary structures such as G-quadruplexes, i-motifs, or triplexes. Such structures would be expected to show complex folding kinetics analogous to what is seen for RNA and proteins. We show here that such is the case for the folding of the human telomere sequence 5′ $AGGG(TTAGGG)_3$ (and variants) into a quadruplex form.

A number of comprehensive reviews of quadruplex DNA structure, function, and suitability as a drug target have been published [12–17]. Among the biologically important G-quadruplex structures are those found at the ends of human telomeres. The single-stranded overhang of telomeres consists of up to 30 tandem TTAGGG repeats [18–23]. It has recently been shown that quadruplexes are found in cells at the ends of telomeres [24–27]. The fundamental building block of the quadruplex is the G-quartet, which consists of four guanine residues linked together by eight hydrogen bonds to form a nearly planer tetracyclic structure with a central cavity [28]. The guanine O6 atoms that project into the G-quartet central cavity coordinate monovalent cations such as $Na^+$ or $K^+$. Thus, cations contribute to the remarkable thermal stability of quadruplexes by neutralizing the partial negative charges of the oxygen atoms [29].

NMR and X-ray crystallographic studies have shown that intramolecular quadruplexes fold into a variety of topologies depending on cation identity, number of G runs, loop sequences, and lengths, as well as 5′ and or 3′ sequences that may interact by base stacking with the main body of the quadruplex [14,30–32]. The human telomere sequence d[$AG_3(TTAGGG)_3$] (Tel22) forms an antiparallel basket structure in $Na^+$ solutions [33] but is found as a "propeller" structure in crystals containing $K^+$ [34]. Although formation of the propeller is promoted by addition of co-solvents such as acetonitrile [35] or polyethylene glycols [36], it is unlikely to be the predominant topology of Tel22 under physiologically relevant conditions [25,36–38]. NMR studies show that modification of the Tel22 sequence by adding 5′ and 3′ extensions such as TT/TA and A/TT, respectively, stabilizes hybrid parallel + antiparallel topologies consisting of two lateral loops and one side-chain reversal loop in $K^+$ solutions [39–43]. In the hybrid-1 state exemplified by d[$TTG_3(TTAGGG)_3A$] (2GKU), the 5′ loop is in the reversed configuration [41], while in the hybrid-2 state, the 3′ loop is reversed {exemplified by 2JSL, d[$TAG_3(TTAGGG)_3TT$]} [43]. It is currently not known which, if any, of these topologies is found in single-stranded telomeric DNA *in vivo*, although recent high-resolution NMR studies designed to mimic conditions within the cellular nucleus suggest a mixture of 2-tetrad antiparallel and 3-tetrad hybrid-2 structures [25].

Folding and unfolding kinetic studies are important for understanding the folding landscape of G-quadruplex formation. There is currently no consensus pathway for folding of monomolecular G-quadruplexes. Based on molecular dynamic simulations of potential folding intermediates, Mashimo and Sugiyama suggested the possibility that formation of hybrid-1 and hybrid-2 quadruplexes could reasonably proceed through an ensemble of hairpin intermediates to chair states followed by strand rearrangement to form type-1 or type-2 quadruplex structures (Fig. 1a) [44]. Later, the same group proposed folding through a triple-helix intermediate (Fig. 1b) [45]. Ambrus *et al.* also suggested a role for a triplex intermediate in the transition from the basket topology in $Na^+$ to the hybrid topology in $K^+$ [39]. In addition, UV photocrosslinking studies of Tel22 in $K^+$ solution provide evidence for the presence of an antiparallel chair conformation and, possibly, triple-helical structures in a dynamic equilibrium [46].

A recent structural dynamics study by Stadlbauer *et al.* on late-stage folding intermediates shows that an important aspect of folding is the correct distribution of *syn* and *anti* G residues in all four strands for an individual molecule to achieve proper folding [47]. This

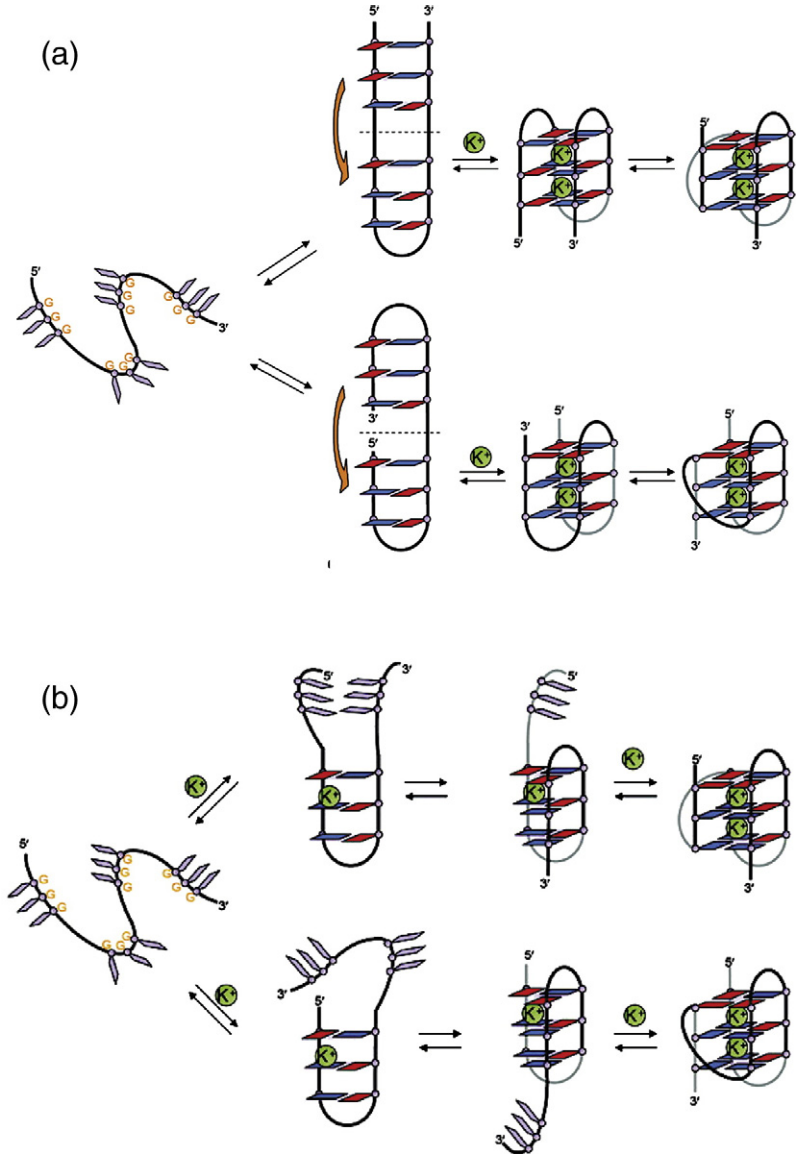


**Fig. 1.** Proposed folding mechanisms for formation of type-1 and type-2 quadruplexes [39,44,45]. Figure adapted with permission from Mashimo *et al.* [45].

is reminiscent of the rate-limiting role of *cis–trans* isomerization of proline peptide bonds in protein folding. These authors concluded that folding is "an extremely multi-pathway process" and likely to be slowed by frequent mis-folding traps. Triplex states of telomeric DNA have been reported in equilibrium studies of 3-tandem repeats of the telomeric sequence [48]. Quadruplex thermal unfolding appears to proceed through a stable triplex intermediate [49–51]. Single-molecule studies of An *et al.* have been interpreted to indicate that the triplex state of a hybrid-2 form is significantly populated at 37 °C [52]. Single-molecule studies of quadruplex dynamics [53,54] complement ensemble kinetic studies and reveal complex dynamic behavior. Single-molecule studies, while informative, have at least two potential drawbacks compared to ensemble studies when attempting to define quadruplex folding pathways. First, the time resolution of published studies is limited and may not capture folding events that are faster than 10 s. Second, published studies of necessity utilized a variety of constructs in which the quadruplex sequence of interest was tethered to duplex DNA. Formation of a quadruplex–duplex conjugate may alter the kinetic and thermodynamic properties of the quadruplex relative to the untethered quadruplex used in ensemble studies, making direct comparison of kinetic parameters difficult [55,56]. Both single-molecule and ensemble kinetic studies of quadruplex folding nevertheless show multiple intermediate states and indicate complex folding pathways.

$$U \underset{k_{-1}}{\overset{k_1}{\rightleftarrows}} I_1 \underset{k_{-2}}{\overset{k_2}{\rightleftarrows}} I_2 \underset{k_{-3}}{\overset{k_3}{\rightleftarrows}} I_3 \underset{k_{-4}}{\overset{k_4}{\rightleftarrows}} F$$

**Scheme 1.** Proposed folding mechanism for the human telomere quadruplex.

Kinetic studies coupled with structure-specific probes can test the folding models from the computational studies outlined above. Experimentally, folding can be initiated by rapidly jumping from unfolding to folding conditions by increasing $K^+$ concentration. The kinetics of unfolding can be assessed by trapping the unfolded state in stable duplex form. In general, irrespective of the cation used or the sequence of the quadruplex-forming DNA, multi-exponential kinetics for both folding and unfolding of monomeric quadruplexes has been observed. This kinetic complexity implies the presence of intermediates and/or multiple folding pathways. For example, we found that the rate of quadruplex folding exhibits a nonlinear dependence on cation concentration, minimally implying a two-step process in which formation of an intermediate becomes rate limiting at high cation concentration [57]. Taking into account the suggestion of Mashimo and Sugiyama [44], we suggested that the intermediate consists of an ensemble of "prefolded" hairpins stabilized by G–G hydrogen bonding. Similar saturation kinetics has been recently observed by Zhang and Balasubramanian in DNA and RNA quadruplex folding [58]. Subsequent experiments in which folding was monitored by changes in the fluorescence of 2-aminopurine (2-AP)-substituted derivatives of Tel22 revealed slower relaxations involving the TTA loops that were not observed by UV spectroscopy [59]. In addition, our kinetic study of the conversion of the $Na^+$ basket form to $K^+$ hybrid states followed by circular dichroism (CD) was interpreted to indicate that the transformation was bi-exponential, revealing the importance of intermediate states [60].

The purpose of the present study is to utilize a variety of spectroscopies to follow the kinetics of folding and unfolding under a uniform set of conditions to characterize intermediate states. The kinetics of quadruplex folding was assessed by mixing unfolded oligonucleotide in buffer with KCl by either stopped flow or manual mixing. The extent of folding was monitored by changes in CD signal, 2-AP fluorescence, or fluorescence resonance energy transfer (FRET) efficiency. CD is sensitive to the geometry of quartet stacking, and quadruplexes with different topologies have distinct spectroscopic signatures. Substitution of fluorescent 2-AP for A in the TTA segments tracks changes in loop rearrangement, and end-labeled FRET efficiency is sensitive to the relative positions of the 5′ and 3′ termini of the oligonucleotide. By comparing the time course of folding using these spectroscopies, we can monitor global folding and changes occurring at specific sites within the molecule. The kinetics of these changes and their wavelength dependence can be related to the appearance and decay of specific structural types. We utilized the following three sequence variants: d[AGGG(TTAGGG)$_3$] ("Tel22"); d[TTGGG(TTAGGG)$_3$A] ("2GKU"); d[TAGGG(TTAGGG)$_3$TT] ("2JSL"). Tel22 folds into a mixture of hybrid forms while 2GKU is enriched in the "hybrid-1" form and 2JSL is enriched in the "hybrid-2" form. All three sequences show equally complex kinetics, indicating that all fold by a multistep reaction mechanism rather than by parallel reactions arising from conformational heterogeneity. We identify previously unreported slow kinetic steps in the folding pathway and obtain time-resolved spectra of intermediate states that provide clues about their conformations. The kinetics will be shown to be consistent with the four-step mechanism shown in Scheme 1, where U represents unfolded oligonucleotide conformers; $I_1$, $I_2$, and $I_3$ are intermediates; and F is the folded state. (The participation of potassium ions is neglected.) It is understood that all of the species in Scheme 1 (with the possible exception of the fully folded structure F) may represent ensembles of related conformers rather than pure single species.

## Results

### Quadruplex folding kinetics monitored by CD

#### *$K^+$-induced folding proceeds through a rapidly formed, short-lived antiparallel intermediate*

Figure 2a and b shows the kinetics of $K^+$-induced folding of Tel22 monitored by stopped-flow CD at 285 nm and 265 nm, respectively. The changes in CD signal at both wavelengths are multiphasic, consisting of relatively rapid changes in ellipticity completed within 1–2 s after addition of KCl followed by much slower changes that require ~$10^4$ s (~2.8 h) to complete. The CD signal at 285 rapidly increased during the initial 1–2 s while that at 265 initially decreased and then slowly increased. The two data sets were fit as described in Methods to a sum of exponentials [Eq. (1)] in which the signal amplitudes and time constants were adjusted to produce the best fit. Three exponentials were required to accurately describe these data (see the distribution of residuals in the upper charts) of Fig. 2a and b. The reaction progress curves calculated using

the least-squares optimized parameters (summarized in Supplementary Table S2) are shown by the red lines in Fig. 2a and b. The relaxation times at 285 nm are 0.104 ± 0.004 s, 0.87 ± 0.11 s, and 1508 ± 28 s; at 265 nm, the relaxation times are 0.26 ± 0.02 s, 128.2 ± 15.6 s, and 2192 ± 115 s. In contrast to the CD progress curves in Fig. 2, which required ~$10^4$ s to complete, stopped-flow experiments in which folding was monitored by multiwavelength UV spectroscopy were ~95% complete by 2 s [57].

To aid in defining the structure of this intermediate, we determined the CD spectrum of the species formed during the initial 2 s subsequent to KCl addition. To accomplish this objective, we carried out stopped-flow kinetic experiments covering this time period at 5-nm intervals over the wavelength range 240–305 nm. The resulting kinetic data (Fig. S1) were fit to a single-exponential relaxation and the signal amplitude at each wavelength was converted to a Δε value as described in Methods (Table S1). The result of this series of experiments is shown by the spectrum depicted in blue in Fig. 2c, which has a peak near 295 nm and a trough near 260 nm. The spectrum clearly differs from the equilibrium CD spectrum in red that represents the fully folded hybrid conformation. The 295 peak and the 260-nm trough of the intermediate are characteristic of antiparallel "basket" or "chair" forms [61]. We therefore conclude from these spectra that an early step in the folding pathway of the human telomeric DNA monomer is formation of an antiparallel intermediate with either a chair or a basket topology. Previous kinetic experiments [57] have shown that the first step in the folding pathway in Scheme 1 involves rapid formation of $I_1$, which consist of rapidly formed intramolecular hairpins. The kinetic CD spectra suggest that formation of intermediate $I_2$ involves collapse of these hairpin-like structures to folded quadruplexes that adopt an antiparallel topography.

Oligonucleotides 2GKU and 2JSL exhibit similar kinetics of folding in 25 mm KCl. As mentioned above, these oligonucleotides fold in $K^+$ solution into hybrid-1 and hybrid-2 conformations, respectively [43], and therefore test the generality of the telomeric quadruplex folding pathway. Comparable experiments showing the complete time course for folding of

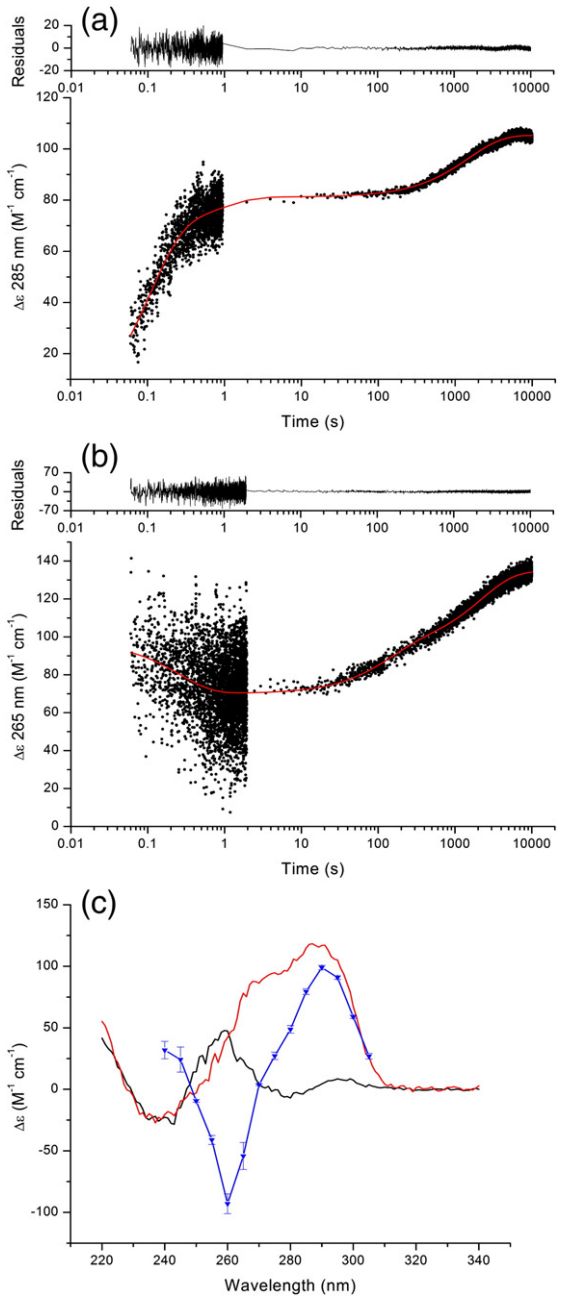


**Fig. 2.** Kinetics of $K^+$-induced folding of Tel22 determined by stopped-flow CD at 285 nm and 265 nm. The data points in (a) and (b) represent the time-dependent change in molar ellipticity at 285 nm (a) and 265 nm (b). To adequately represent the complete time course, we collected separate data sets covering fast and slow kinetic processes (with different digital integration times). The two data sets were combined and fit to a sum of three exponentials [Eq. (1), $i = 3$]. The red lines in (a) represent progress curves calculated from the best-fit parameters given in Supplemental Table S1. The upper chart shows the distribution of residuals for the fit of each data set. (c) The calculated CD spectrum (blue) of the species present 2 s after a 0 → 25 mM $K^+$-jump compared to the CD spectrum before KCl addition (black) and the spectrum scanned ~24 h after KCl addition (red). The kinetic spectrum was calculated by fitting individual kinetic data sets covering the initial 2 s of folding to a single exponential [Eq. (1), $i = 1$]. The raw data and the fits are shown in Fig. S1. The resulting wavelength-dependent CD signal amplitudes were normalized to the concentration of Tel22 and the 0.2-cm path length of the observation cell. The error bars represent the error in the fitted signal amplitudes. Conditions: Tel22 (43 μM in t-$Bu_4$AmP folding buffer) was mixed at ~22 °C in a 1:1 ratio with 50 mM KCl by stopped-flow.

2GKU and 2JSL initiated by a 25 mM KCl jump assessed by stopped-flow CD are shown in Figs. S2 and S3. These kinetic CD spectra (Fig. S4) show that both 2GKU and 2JSL pass through a similar antiparallel intermediate as Tel22. Moreover, addition of 5′ and 3′ flanking sequences to the core quadruplex sequence decreases the rate of formation of the antiparallel intermediate with the rate following the order Tel22 > 2GKU > 2JSL (Figs. S5 and S6 and Tables S1 and S2).

### *Manual $K^+$-jump experiments allow assignment of CD spectra to intermediate $I_3$*

The stopped-flow CD experiments in Fig. 2a and b covering the time period $10^{-2}$ s to $10^4$ s showed that the rapid CD changes were complete by ~10 s after KCl addition and that slower changes in CD signal occurred between $10^2$ s and $10^4$ s. These changes are slow enough that complete CD spectra could be recorded using the interval scan mode of the CD spectrophotometer after manually mixing the unfolded oligonucleotide with a small aliquot of concentrated KCl. The dead time of these manual mixing experiments, from addition of a cation to initiation of data collection, is 7–10 s. The kinetic data collected consist of CD spectra from 320 nm to 220 nm recorded at 41-s intervals over $10^4$ s. The resulting data matrices consisting of time-dependent CD spectra were analyzed to determine kinetic constants and species spectra by singular value decomposition (SVD) using the program GlobalWorks (see Methods).

SVD analysis and fitting the resulting significant kinetic eigenvectors to a variety of plausible mechanisms showed that three spectrally significant species were required to describe the wavelength and time dependence of the spectral changes associated with folding of each of the three oligonucleotides Tel22, 2GKU, and 2JSL. The significant kinetic eigenvectors were globally fit to a two-step relaxation corresponding to the pathway in Scheme 1 in which the initial step ($\tau < 1$ s) is completed during the 5- to 7-s dead time. Thus, we expect to see only the last two folding steps: $I_2 \rightarrow I_3 \rightarrow F$. As noted below in Data analysis, the assignment of a rate constant to a particular step in a sequential reaction is ambiguous in that solutions to the least-squares fitting algorithm with either $k_2 > k_3$ or $k_2 < k_3$ will produce equally good fits [62,63]. Additional chemical or spectroscopic information is required to determine which step is rate determining. Here, we assume (justified below) that conversion of $I_2$ to $I_3$ is slower than conversion of $I_3$ to F. Figure 3a shows the results of fitting the kinetic eigenvectors derived by SVD to a two-exponential expression. The top chart shows the residuals of the fitted progress curve, and the center chart shows the calculated kinetic profiles of the eigenvectors associated with each of the three species. For Tel22 in 25 mM KCl at 25 °C, the relaxation from $I_2$ to $I_3$ proceeds with a time constant of ~3700 s and the conversion of $I_3$ to F takes place with a time constant of ~760 s.

Given a specific mechanism, the SVD analysis in conjunction with the fitted parameters allows calculation of the CD spectra of the kinetically significant species. Figure 3b shows the derived spectra of the

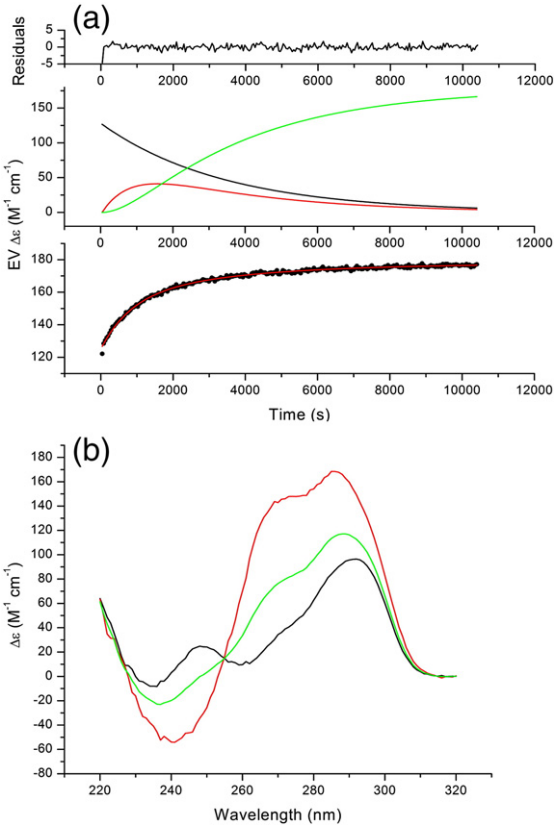


**Fig. 3.** Formation kinetics and CD spectra of Tel22 folding intermediates during KCl-induced quadruplex formation. Folding was initiated by manually mixing a small volume of 3 M KCl with Tel22 in folding buffer. CD spectra were recorded prior to KCl addition and at 41-s intervals thereafter for $10^4$ s. The spectra were assembled into a data matrix that was analyzed with the SVD and nonlinear least-squares kinetic fitting modules of the program GlobalWorks. The data points in the bottom chart in (a) represent the amplitude of the most significant eigenvector and the red line represents the best fit to a sum of two exponentials [Eq. (1), $i = 2$] calculated using the best-fit rate constants $k_1 = (2.7 \pm 0.5) \times 10^{-4}$ $s^{-1}$ and $k_2 = (1.31 \pm 0.20) \times 10^{-3}$ $s^{-1}$ ($\tau_1 = 3700$ s and $\tau_2 = 760$ s). The middle chart shows the temporal profile of the starting, intermediate, and final species (black, red, and green lines, respectively). The top chart shows the residuals of the fit. (b) The calculated spectra of the starting (black), intermediate (red), and final states (green). Since the dead time of the manual mixing experiment is 41 s, the spectrum of the starting state consists of a mixture of the rapidly formed (2-s) I1 state in Fig. 2 and the intermediate I2 that starts to form during the initial 41-s period before complete recording of the first spectrum after KCl addition occurred. Conditions: [Tel22] = 4.8 μM, [KCl] = 25 mM, temperature = 25 °C.

three kinetically significant species. The calculated spectrum of species A (black line) resembles a mixture of unfolded Tel22 and the 1-s antiparallel spectrum (note the negative ellipticity at 260 nm) with a species with positive ellipticity at 260 nm and 290 nm. This spectral mixing arises because recording of the CD full spectrum required 42 s and both species will be present during this time period. The CD spectrum of species B (red line) exhibits a large positive ellipticity at 260 nm. This spectrum is similar in shape and magnitude to the CD spectrum of an intermediate previously identified as a triplex intermediate in the thermal denaturation of Tel22, 2GKU, and 2JSL [50]. We use this similarity to justify the choice of $k_2 < k_3$ in the fitting procedure. The alternative $k_2 > k_3$ yielded significantly different intermediate spectra. Lastly, species C (green line) matches that of the fully folded equilibrium spectrum for Tel22 in KCl. Similar experiments with 2GKU and 2JSL in which folding was initiated by manual addition of 25 mM KCl and monitored by CD wavelength scanning are presented in Fig. S7. Folding of these oligonucleotides was also bi-exponential with similar kinetic constants as Tel22. The calculated CD spectrum of the intermediate $I_3$ shown in Fig. S7b and d for 2GKU and 2JSL also exhibited a peak (2JSL) or a shoulder near 260 nm (2GKU).

In summary, the complete time courses for $K^+$-induced folding of Tel22, 2GKU, and 2JSL determined by changes in CD, are compared in Fig. S6. All sequences show slow and complex folding pathways, but the rates of folding clearly differ with Tel22 folding most rapidly and with 2JSL folding most slowly.

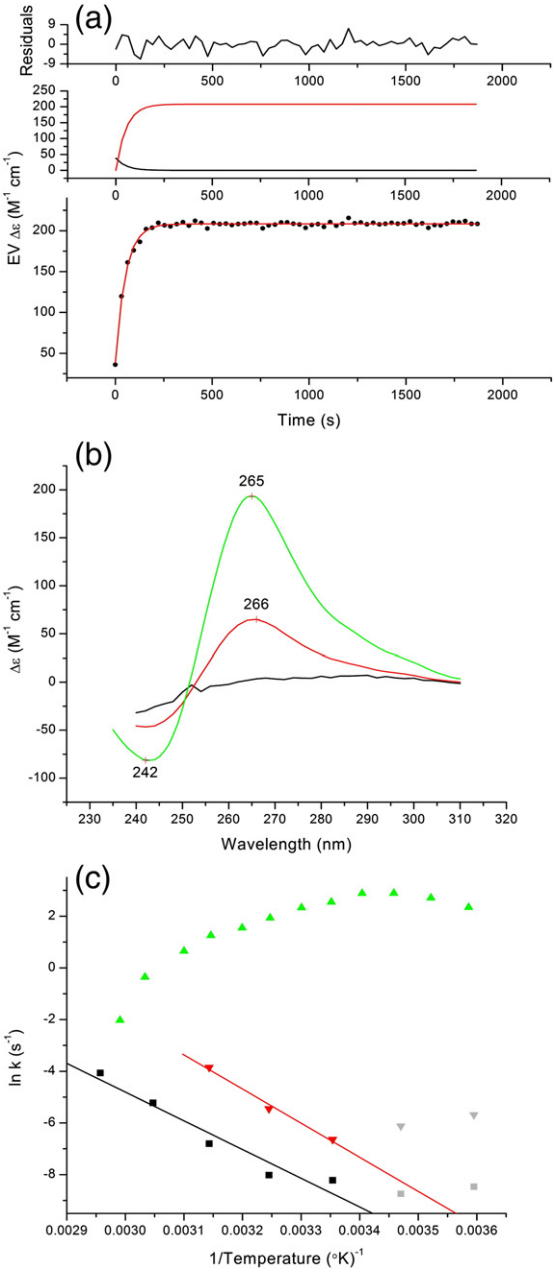


**Fig. 4.** Temperature dependence of the kinetics of Tel22 $I_3$ formation determined by wavelength scanning CD spectroscopy. In (a) and (b), folding was initiated at 65 °C as described in Fig. 3 by manual addition of KCl to give a final $K^+$ concentration of 25 mM. The resulting data matrix was analyzed by SVD. (a) The most significant kinetic eigenvector (data points in the middle chart) could be adequately fit to a single exponential (red line) with a first-order rate constant of $(1.89 \pm 0.01) \times 10^{-3}$ $s^{-1}$ ($\tau = 59.3$ s). Similar kinetic experiments carried out at lower temperatures were biphasic. (b) The CD spectra of the starting (unfolded) species (black line) and the final folded species (red line) at 65 °C calculated from the SVD analysis of the kinetic data in (a). Shown in green for comparison is the CD spectrum of a proposed triplex intermediate formed in the temperature-induced unfolding of Tel22 [50]. (c) Arrhenius plots for formation $I_3$ (putative triplex, black squares) and the folded state (F, red triangles). For comparison, the green triangles represent rate constants for Tel22 folding in 25 mM KCl determined by stopped-flow UV spectrophotometry. Linear regression (red and black lines with points in gray omitted from the regression analysis) allows estimation of the Arrhenius activation energies for formation of $I_3$ and F to be 22 kcal/mol and 26 kcal/mol, respectively. The nonlinear plot shown by the green triangles was previously interpreted to indicate that the folding kinetics assessed by UV absorption consists of more than one step [57].

### *Formation of intermediate $I_3$ has a high activation energy*

Our previous kinetic studies on the $K^+$-induced folding of Tel22 and 2GKU monitored by stopped-flow UV spectroscopy in 50 mM KCl gave nonlinear Arrhenius plots, probably resulting from a change in the rate-limiting step with temperature [57]. In the current series of experiments, the nonlinear Arrhenius behavior was confirmed for Tel22 in 25 mM KCl in the temperature range 5–55 °C (green triangles in Fig. 4c). The relatively slow rate of $I_3$ formation and its conversion to F allowed us to use manual addition

of KCl in conjunction with wavelength scanning CD to estimate the activation energy for these two steps in the folding process. Our previous thermal unfolding studies of Tel22 in 25 mM KCl [50] indicate that $I_3$ should be the predominant "folded" species in the temperature range of ~50 to ~80 °C. The results of a $K^+$-jump conducted at 65 °C (where ~60% of the mixture should consist of $I_3$ and ~40% unfolded) as analyzed by SVD are shown in Fig. 4a. At 55 °C and above, the kinetics of folding could be adequately fit to a single exponential representing the formation of $I_3$ from unfolded structures. The calculated CD spectrum of the product at 65 °C (red line) resembles the calculated CD spectrum of the previously described melting intermediate [50]; both have maxima near 265 nm and minima near 240 nm. However, the magnitude of the kinetic spectrum is less than that of the thermal intermediate, a result that is readily explained if, as expected, the kinetic spectrum consists of a mixture of folded and unfolded species at this temperature. At temperatures between 25 and 55 °C, two exponentials were required to fit the kinetic data. Presumably, these two phases represent formation of $I_3$ and its subsequent conversion to the folded state. From the linear segments of the Arrhenius plots in Fig. 4c, we estimate activation energies of ~22 kcal/mol for formation of $I_3$ from U and ~26 kcal/mol for the conversion of $I_3$ to F.

## Folding kinetics monitored by FRET

Attachment of a suitable fluorescence donor and acceptor to the 5′ and 3′ ends of a quadruplex allows monitoring folding by observing changes in FRET that accompany movement of terminal residues to their equilibrium position in the folded quadruplex. The labels 6-carboxyfluorescein (6-Fam) and 5-carboxytetramethylrhodamine (Tamra) attached by 6-carbon linkers to the 5′ and 3′ ends, respectively, of Tel22 respond to cation-induced quadruplex folding by donor fluorescence quenching (observable at 520 nm) and acceptor fluorescence enhancement (observable at 590 nm) when the donor is excited at 490 nm.

## Stopped-flow folding kinetics

To monitor the changes in FRET for comparison with the kinetics of CD changes, we carried out stopped-flow $K^+$-jump experiments in which the 6-Fam donor was excited and the emission intensity of the donor was assessed using a band pass filter at positioned perpendicular to the exciting light beam. Figure 5 shows the time course of 6-Fam fluorescence quenching when the oligonucleotide 6-Fam-Tel22-Tamra was mixed with KCl to give a final $K^+$ concentration of 25 mM. There was rapid fluorescence quenching during the ~5-ms dead time of the stopped-flow apparatus. Slower relaxations of 0.75 s, 2.3 s, and 23 s followed the initial rapid quenching step. We also observed slow photobleaching of the 6-Fam residue that accounted for the slow decrease in fluorescence at the longer observation times. We corrected for this zero-order process in the fitting expression [Eq. (1) and Methods].

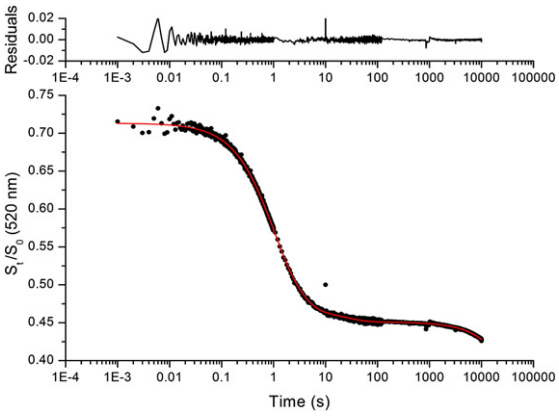


**Fig. 5.** Kinetics of quadruplex folding of 6-Fam-Tel22-Tamra determined by quenching of 6-Fam fluorescence due to changes in FRET efficiency. To capture the complete reaction, we collected individual data sets for 0–2 s, 0–120 s, and 0–$10^4$ s. The sets were merged to produce a composite data set covering the time span 0–$10^4$ s. The fluorescence intensity was normalized to the intensity measured independently by mixing the oligonucleotide with buffer. The resulting normalized data set was fit to a sum of three exponentials plus a zero-order (linear) correction for photobleaching [Eq. (1), $i = 3$]. The points represent the data and the red lines represent the calculated time course using the best-fit parameters listed in Supplementary Table S4. Excitation was as 490 nm (6-Fam) and emission was detected at 90° through an interference filter with peak transmittance at 520 nm. Oligonucleotide concentration, 0.9 μM; [KCl], 25 mM after stopped-flow mixing. Temperature, 25 °C.

## Tamra emission spectra of kinetic intermediates

To define the fluorescence properties of the intermediates observed by stopped-flow mixing, we conducted manual KCl addition experiments in which the emission spectrum of the FRET acceptor Tamra was recorded at 14-s intervals for the time period 20 s to $10^4$ s. Exciting 6-Fam at 490 nm ensured that Tamra emission resulted exclusively from FRET. Since the dead time is ~20 s, we expect that the rapid quenching of 6-Fam fluorescence seen in Fig. 5 that occurred during the initial 10 s after the [$K^+$] jump should have been completed before the start of wavelength scanning. The resulting time-dependent emission spectra were assembled into a wavelength *versus* time matrix that was analyzed by SVD to determine the minimum number of kinetically significant species and their emission spectra. The results of this analysis for 6-Fam-Tel22-Tamra

folding in 25 mm KCl are shown in Fig. 6. Similar experiments for 2GKU and 2JSL are in Fig. S9. Least-squares fitting of the Tel22 data set required two exponentials with rate constants of (1.4 ± 0.3) × $10^{-4}$ $s^{-1}$ and (6.7 ± 0.8) × $10^{-4}$ $s^{-1}$ (relaxation times of 7100 s and 1490 s). As discussed above, since the rapid component (attributed to formation of $I_2$) is complete within the 20-s dead time, we assign the slower relaxation (7100 s) in Fig. 6a to conversion of $I_2$ to $I_3$ and the more rapid relaxation (1490 s) to the conversion of $I_3$ to the folded state, F. The calculated Tamra emission spectra for the kinetically significant species are shown in Fig. 6b. The 590-nm emission intensity of $I_3$ is significantly greater than that of $I_2$ or F. At first glance, this increase in acceptor emission may seem incompatible with formation of a triplex state since we expect a decrease in FRET efficiency as the distance donor and acceptor increases, as it might upon formation of a triplex state. To explain this apparent inconsistency, we cite previous studies showing Tamra fluorescence is quenched by distance-dependent charge transfer to guanine in oligonucleotides [64–66]. Thus, it is possible that the increase in Tamra fluorescence associated with $I_3$ results from an increase in the distance between the 3′-Tamra fluorophore and guanine residues rather than a change in FRET. Indeed, the data in Fig. 5 show minimal quenching of 6-Fam fluorescence after ~100 s.

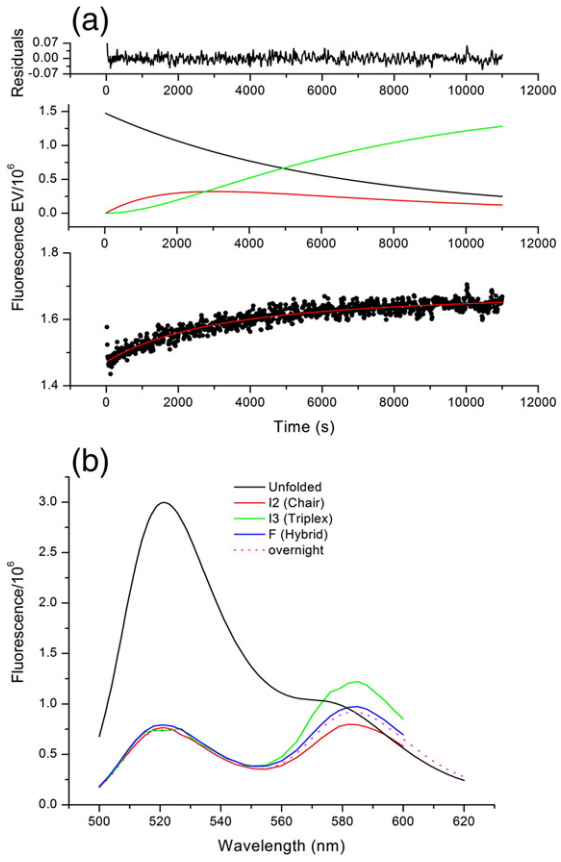


**Fig. 6.** Kinetics of quadruplex folding assessed by changes in the fluorescence emission spectrum of 6-Fam-Tel22-Tamra. (a) The results of SVD analysis and least-squares fitting the kinetic eigenvectors to a sum of two exponentials using the program GlobalWorks described in Methods. The red line in the lower chart represents the time course calculated with the best-fit rate constants of $k_1$ = (1.7 ± 0.4) × $10^{-4}$ $s^{-1}$ and $k_2$ = (5 ± 3) × $10^{-4}$ $s^{-1}$ ($\tau_1$ = 5880 s and $\tau_2$ = 2000 s). The center chart shows the kinetic profile of the eigenvectors representing each kinetic species. The upper chart shows the residuals of the fit. (b) The calculated emission spectra of the kinetically significant species $I_1$, $I_2$, and F and compares them with the experimentally determined spectra of the unfolded (U) and equilibrium folded ensembles (F). Fluorescence intensity is in units of counts per second.

Electron transfer between excited Tamra and guanine residues also explains why the donor and acceptor emission time profiles are not symmetrical. This asymmetry, which is manifested in the different kinetic profiles for changes in emission intensity of the donor and acceptor moieties shown in Fig. 8, no doubt reflects differences in the photophysics of this donor–acceptor pair within the context of the guanine-rich oligonucleotides. In particular, acceptor emission intensity depends on contributions not only from FRET but also on a distance-dependent quenching resulting from Tamra-guanine proximity, while quenching of donor fluorescence depends only on the topological relation between donor and acceptor.

## Folding kinetics monitored by 2-AP fluorescence

Substitution of 2-AP for adenine incorporates a fluorescent reporter residue that can be used to monitor conformational changes at specific locations such as in the TTA loops in quadruplex model oligonucleotides. The fluorescence quantum yield of 2-AP is highly sensitive to factors such as nearest sequence neighbors, base stacking, and interaction with solvent [67–72]. In an earlier study [59], we found that, when followed for 1200 s, $K^+$-dependent folding of Tel22 exhibited two relaxations in the 40–900 s time range. Depending on the position of the loop, the quantum yield of the intermediate states increased or decreased with respect to that of the unfolded structure.

In the current set of experiments, we extended the time of observation to encompass the $10^4$ s time span used in the CD and FRET experiments. The results of these experiments for the four 2-AP-substituted oligonucleotides of Tel22 are shown in Fig. 7. The kinetic profiles reveal that each of the substitutions except AP1 show significant changes in fluorescence over the initial 2 s that coincide with formation of the antiparallel structure detected by CD. For AP7 and AP19, the fluorescence increases relative to the unfolded state, while for AP13, there is

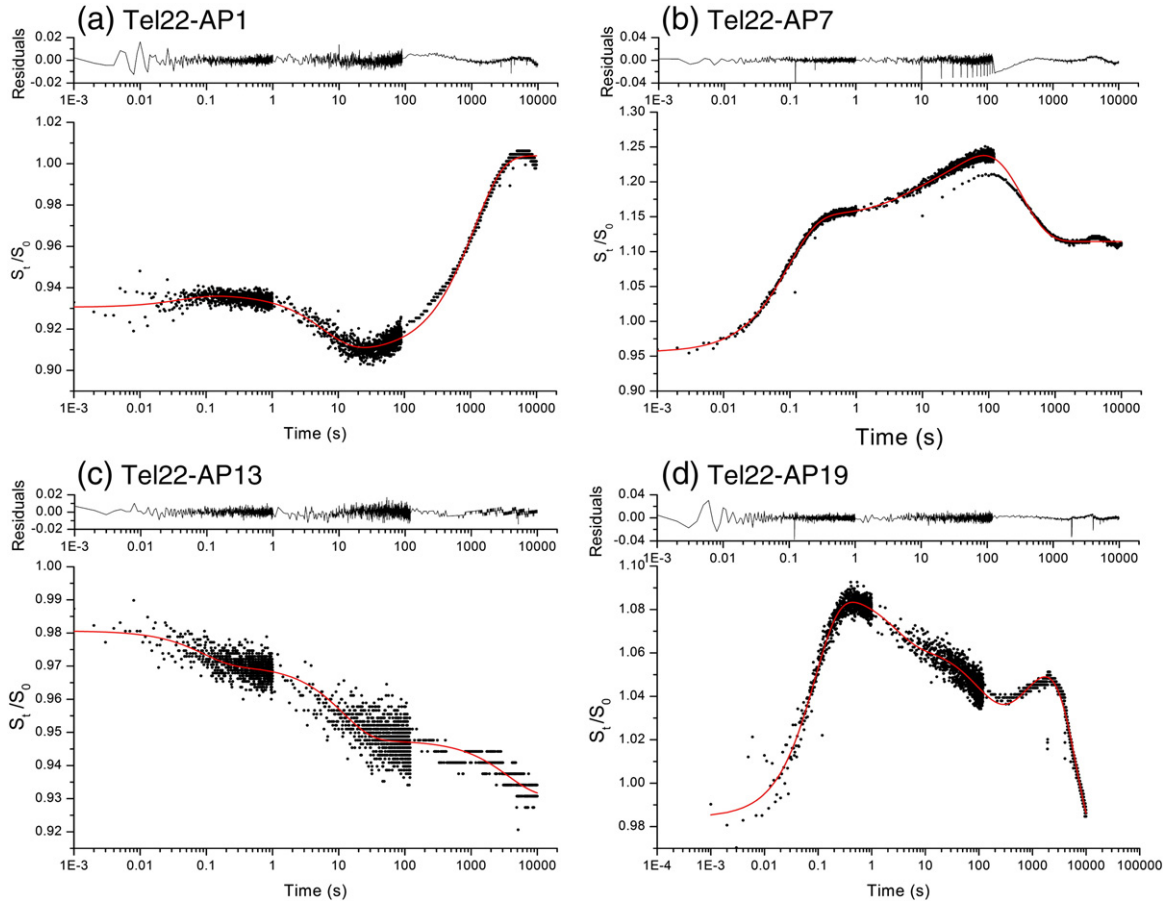


**Fig. 7.** Kinetics of changes in 2-AP fluorescence induced by $K^+$-jump for the dA → d2-AP derivatives of Tel22. The overall time course of fluorescence change is a composite of three separate kinetic runs spanning the three time ranges: 0–2 s, 0–120 s, and 0–$10^4$ s. $S_t/S_0$ is the ratio of the fluorescence intensity at time $t$ to that measured independently at $t = 0$. The red lines were calculated from parameters obtained by fitting the data points to a sum of three or four exponentials [Eq. (1), $i = 3$ or $i = 4$]. The best-fit parameters are summarized in Supplementary Table S5. Residual plots for the fits are shown in the upper part of each panel. Conditions: 2-AP excitation was at 305 nm and fluorescence emission was observed at right angles through a 320-nm-cutoff filter. [Tel22-AP1] = 5.2 μM, [Tel22-AP7] = 5.8 μM, [Tel22-AP13] = 6 μM, [Tel22-AP19] = 6.5 μM, [KCl] = 25 mM after mixing. Temperature = 25 °C.

a small decrease in fluorescence. For AP1, AP13, and AP19, fluorescence is quenched is a second slow step, whereas it is enhanced in AP7. Finally, in the slowest relaxation, there is a major increase in AP1 fluorescence while the fluorescence at the other three positions decreases. Given the variety of factors that influence the quantum yield of 2-AP, it is difficult to assign specific structural changes to the changes in emission intensity. However, regardless of the detailed structural basis for these changes in emission intensity, it is clear that the conformational alterations sensed by CD and FRET are accompanied by adjustments in the individual loops that result in complex changes in 2-AP fluorescence quantum yield.

Figure 8 provides a summary of the folding kinetics observed by different spectroscopies. Complex time courses are observed for the different signals. All share three relaxation times of approximately 0.2 s, 21 s, and 1300 s.

## Unfolding kinetics overview

We next investigated the kinetics of quadruplex unfolding by trapping the unfolded state in the form of a duplex with excess complementary DNA. Since bimolecular duplex formation of oligonucleotides is fast (millisecond timescale), this assay is assumed to reveal a rate-limiting slow step along the unfolding pathway, namely, the exposure of a single-stranded segment to which the complementary strand may hybridize to initiate complete unfolding. Subsequent unfolding events occur on the complementary strand lattice leading to formation of a full-length duplex. It is important to realize that these reactions need not reflect the exact reversal of the folding process but

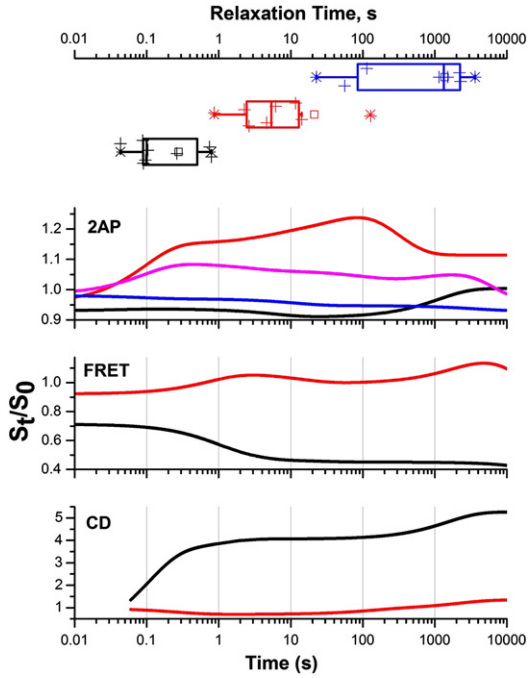


**Fig. 8.** Summary of Tel22 folding kinetics detected by different spectroscopies.

instead represent a separate reaction mechanism. Quadruplex unfolding is slow enough that manual mixing and wavelength scanning could be combined to determine spectroscopic signatures of intermediates using SVD analysis of the wavelength *versus* time data matrices. Selected primary data for Tel22 are shown, with remaining data for difference spectroscopic signals and sequences used shown in Figs. S10 and S11 and Table S6).

## Quadruplex unfolding monitored by FRET

Quadruplex unfolding initiated by trapping with the Tel22 complementary DNA was studied by FRET analysis using both time-dependent changes in steady-state emission spectra and by monitoring changes in donor lifetime. The results of these experiments are shown in Figs. 9 and 10. Three relaxations with time constants 13.5 s, 145 s, and 2000 s (Fig. 9) are observed, with a steady decrease in FRET efficiency. The emission spectra of the species showed the largest change in donor emission at ~520 nm and small changes in acceptor emission at ~590 nm. The observation of a small decrease in Tamra emission compared to the relatively large increase in 6-Fam emission on unfolding can be explained as described above by previous studies showing that Tamra emission is quenched by excited state charge transfer between guanine and the Tamra excited state [64–66]. The rapid increase in donor fluorescence on unfolding that is not accompanied by a significant change in

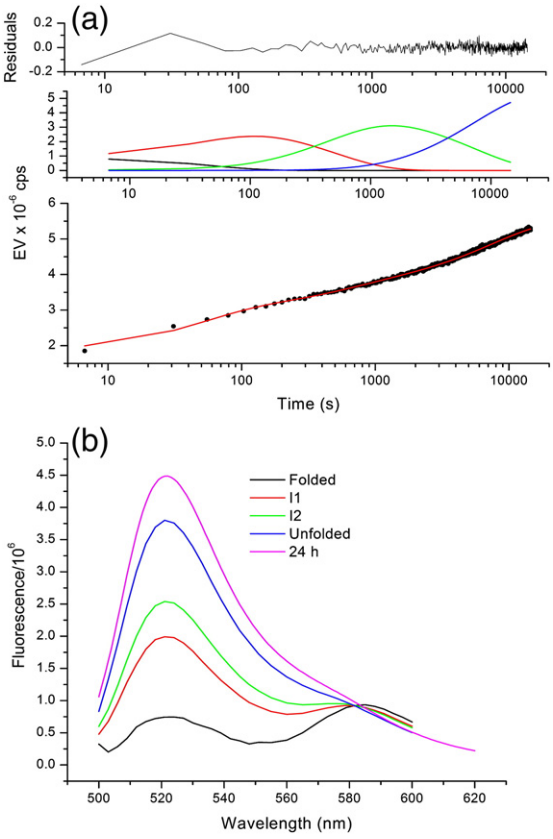


**Fig. 9.** Kinetics of unfolding of 6-Fam-Tel22-Tamra as a function of emission wavelength. The unfolded state was trapped by adding a 5-fold excess of Tel22 complement to 0.5 μM 6-Fam-Tel22-Tamra in 25 mM KCl at 25 °C. Excitation was at 490 nm. Emission spectra were recorded periodically and the resulting time-dependent emission intensity matrices were analyzed by SVD using the program GlobalWorks. The significant eigenvectors representing the data set were fit by nonlinear least squares to a three-exponential sequential reaction mechanism. The bottom graph in (a) shows the experimentally determined data points and the red line shows the time course using the best-fit parameters $k_1 = (7.4 \pm 0.7) \times 10^{-2}$ $s^{-1}$, $(6.9 \pm 1.0) \times 10^{-3}$ $s^{-1}$, and $(5.0 \pm 0.8) \times 10^{-4}$ $s^{-1}$. The corresponding relaxation times are $\tau_1 = 13.5$ s, $\tau_2 = 145$ s, and $\tau_3 = 2000$ s. The top graph in (a) shows the distribution of residuals for the fit in the bottom graph and the center panel shows the formation and decay the folded, I1, I2, and unfolded species over the course of the unfolding reaction. The calculated emission spectra of the folded (black), I1 (red), I2 (green), and unfolded (blue) species, as well as the experimentally determined 24-h emission spectrum (magenta) are shown in (b).

Tamra emission suggests that Tamra is already quenched owing to its proximity to guanine residues until the last step in the unfolding reaction. The slowest relaxation time most probably represents a rate-limiting step in quadruplex unfolding in which an arm is exposed to initiate duplex formation on the complementary trap strand. This might be a triplex

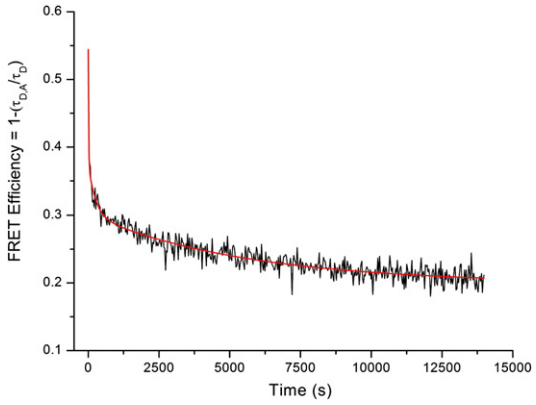


**Fig. 10.** Unfolding of 6-Fam-Tel22-Tamra assessed by time-dependent changes in 6-Fam fluorescence lifetime. The unfolding reaction was initiated by adding a 5-fold excess of Tel22 complement after establishing the fluorescence lifetime of the folded quadruplex. Excitation λ = 468 nm; emission was detected at right angles to excitation using a 520-nm band pass filter. Donor lifetime was assessed using 6-Fam-Tel22 under identical conditions. [6-Fam-Tel22-Tamra] = 0.6 μM, [KCl] = 25 mM, ~22 °C. The data were fit by nonlinear least squares to Eq. (1) ($i$ = 3). The red line is the progress curve calculated using the best-fit parameters $S_\infty$ = 0.199 ± 0.003, $S_1$ = 0.167 ± 0.02, $\tau_1$ = 0.21 ± 0.09 s, $S_2$ = 0.076 ± 0.01, $\tau_2$ = 4 ± 1 s, $S_3$ = 0.103 ± 0.003, $\tau_3$ = 92.1 ± 8.7 s.

intermediate postulated to be $I_3$. The subsequent faster relaxation times represent unfolding of the remaining quadruplex segments and formation of the full-length duplex. These two steps could not be exact reversal of steps along the folding pathway but rather are unique steps in the trap mechanism.

The kinetics of unfolding the FRET derivatives of 2GKU and 2JSL, which consist of single conformers by NMR, were also multiphasic. The rate constants and calculated emission spectra of intermediates are similar to those of Tel22 (Fig. S9). These results confirm that the heterogeneous unfolding kinetics of telomeric DNA quadruplexes result from a complex mechanism rather than structural heterogeneity in the folded quadruplexes.

Measurement of the extent of FRET by determining donor lifetimes in the presence and absence of acceptor provides direct method of calculating Förster transfer efficiency. We therefore carried out lifetime measurements for 6-Fam fluorescence of Tel22 in the presence and absence of the Tamra acceptor over the course of unfolding using a frequency-domain lifetime instrument. The time required to measure the phase and modulation shift is short compared to the time for quadruplex unfolding, thereby allowing us to measure the donor fluorescence lifetime over the course of the unfolding reaction. The results of these experiments are shown in Fig. 10. The kinetics of unfolding expressed as changes in FRET efficiency induced by complement addition were triphasic with similar time constants as determined independently from the emission intensity (Fig. 9). The greatest fraction of the change in efficiency occurred in the initial rapid step ($\tau$ < 60 s), suggesting that a major increase in the distance between donor and acceptor occurs in this step. Studies of Unruh *et al.* indicate that a 6-Fam moiety tethered to the 5′ end of oligonucleotides exhibits free rotation; thus, changes in FRET efficiency most likely result from changes in the distance between donor and acceptor [73,74].

### Multiphasic unfolding monitored by CD and 2-AP fluorescence

Unfolding of Tel22 monitored by changes in 2-AP fluorescence also revealed multiphasic kinetics. These results (shown in Fig. S10) are generally consistent with the results obtained by FRET.

Figure 11 shows a summary of quadruplex unfolding initiated by trapping with the Tel22 complementary DNA. Different spectroscopies all show multiphasic time courses with differing amplitudes for each phase reflecting the global or local responses of the particular signal to the extent of unfolding.

## Discussion

These studies offer the most detailed glimpse to date into the folding of the human telomere G-quadruplex. A previously unobserved slow kinetic phase is reported.

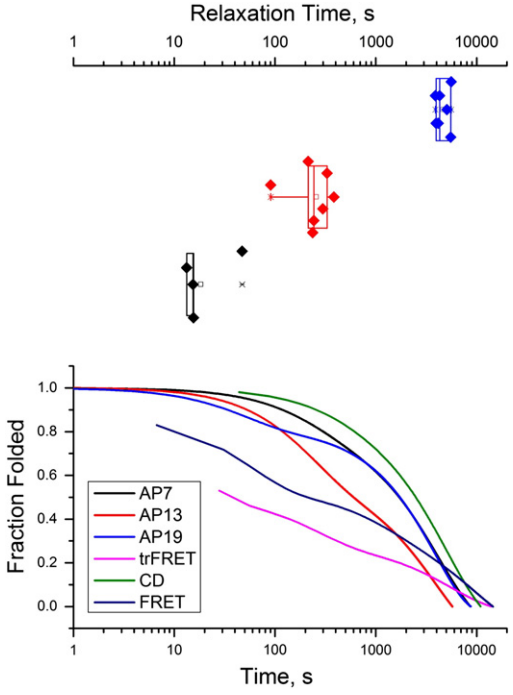


**Fig. 11.** Summary of Tel22 unfolding kinetics monitored by different spectroscopies.

The data show that multiple intermediates exist along the folding pathway. The structures of these intermediates are open to interpretation, but their existence is not. The use of multidimensional spectroscopic methods allows the spectra of intermediate species to be determined, providing clues about their structural features. These kinetic studies are consistent with the scheme shown in Fig. 12 in which folding occurs in four phases by way of antiparallel chair structures and a proposed triple-helix intermediate. The slow, multiphasic kinetics of the folding of the topologically complex quadruplex is more like kinetics observed for RNA and protein folding than for folding of simple duplex hairpin DNA structures.

## Comparison with previous kinetic studies of telomere quadruplex folding

A number of earlier studies provide kinetic evidence for intermediates in the folding of single-stranded G-rich oligonucleotides into quadruplex structures [53,57,58]. Using single-molecule FRET with a suitably labeled quadruplex attached to a duplex tether anchored to a solid-state substrate, Lee *et al.* found a complex mixture of different FRET efficiencies that they interpreted to be a mixture of parallel and antiparallel species [53]. The relative proportions of the species could be manipulated by changes in $K^+$ concentration or temperature. When 2 mM $K^+$ was added to the construct in solution, a biphasic increase in FRET efficiency was observed with relaxation times of 8.8 s and 253 s.

Using multiwavelength stopped-flow absorption spectroscopy, we found that the time course of Tel22 and 2GKU folding assessed at 25 °C initiated by a 50 mM KCl jump was characterized by single relaxation with a time constant τ of ~40 ms for Tel22 and of ~220 ms for 2GKU [57]. In subsequent kinetic studies in KCl with 2-AP substituted for adenine in the loop positions of Tel22 and with folding monitored by changes in 2-AP fluorescence, slower and more complex kinetics than those seen in UV spectroscopy were observed [59]. The relaxation times for the changes in 2-AP fluorescence were site

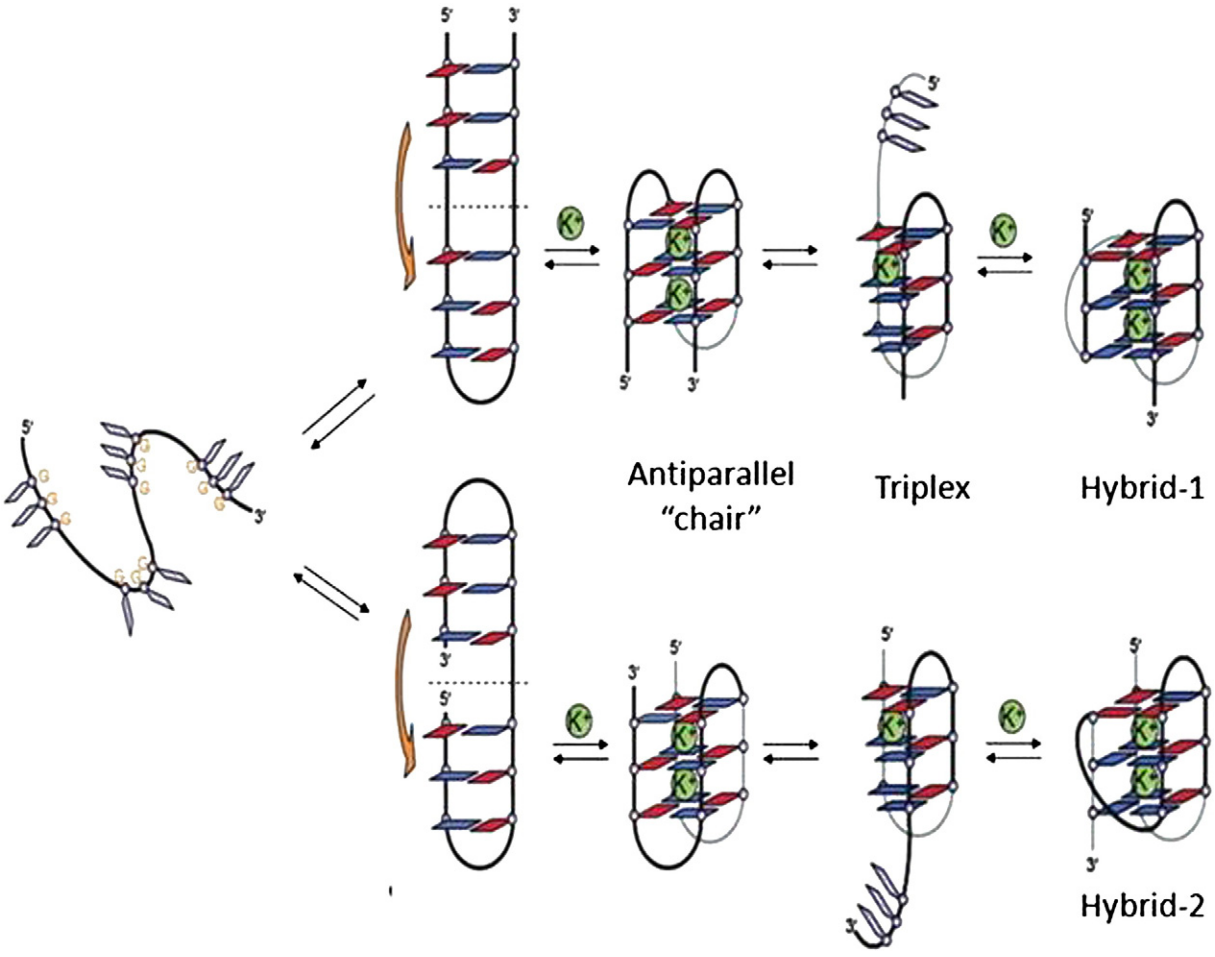


**Fig. 12.** Proposed folding mechanism for human telomere quadruplexes. Figure adapted with permission from Mashimo *et al.* [45].

specific with relaxation times of 1–10 s, ~40 s, and up to 900 s. Recently, Zhang and Balasubramanian compared the kinetics of $K^+$-induced folding of {d[$(GGGTTA)_3GGG$]} with that of several ribonucleotide analogs and reported relaxation times of 7 ms and 40 ms for the DNA quadruplex in 90 mM KCl [58].

Our earlier study showed that the rate constant for step 1 in Scheme 1 exhibits hyperbolic (saturating) dependence on [$K^+$], suggesting that $I_1$ forms in a pre-equilibrium step that becomes rate limiting at high cation concentration [57]. The structure of this intermediate has not been defined, but various authors have suggested hairpin duplexes, slipped duplexes, triplexes, and quadruplexes as indicated in Fig. 1 [44,45,47,58]. We can now provide new spectroscopic clues for the nature of the structures of the intermediates $I_1$, $I_2$, and $I_3$.

## Spectroscopic identification of folding intermediates

### *The U-to-$I_1$ step: Collapse to hairpin ensemble*

FRET studies with 6-Fam-Tamra labeled oligonucleotides are consistent with rapid formation (<5 ms) of structures characterized by partial quenching of the 6-Fam moiety, most probably hairpins in which the terminally labeled residues are brought closer together by cation-induced collapse, thereby resulting in the increased FRET that is manifested in donor quenching. This is shown by the FRET kinetics in Fig. 5 where the initial observable fluorescence signal at 520 nm is reduced by 25% of that expected based on the fluorescence of 6-Fam-Tel22-Tamra in the absence of KCl. In addition, the CD spectrum of Tel22 before addition of potassium (Fig. 2c) differs from the spectrum expected for fully unfolded, single-strand DNA. This indicates the presence of some structures, perhaps hairpins. Simulations have shown that a variety of hairpin and slipped hairpin structures are at least transiently stable [45,47], consistent with our experimental observations.

### *The $I_1$-to-$I_2$ step: Formation of an antiparallel structure*

A major finding of the present study is the spectral characterization of the $I_2$ intermediate (Fig. 2c). We believe that this is the first time that an unambiguous signature spectrum of a rapidly formed intermediate in quadruplex folding has been described. In less than 1 s in 10 or 25 mM KCl, the rapidly formed hairpins fold up to form structures with a CD spectrum characteristic of an antiparallel quadruplex, in particular, group III chair forms described by Karsisiotis *et al.* [61]. Remarkably, the antiparallel CD spectrum was obtained for all three of the telomere analogs that are known to form different final conformations (Tel22-mixture, 2GKU-hybrid-1 and 2JSL-hybrid-2), thereby showing that all three topologies proceed to their final state through a common structural intermediate. These findings argue against the proposed scheme in Fig. 1b in which folding proceeds first through a triple-helical intermediate [45,58]. Moreover, the rapid decrease in donor emission (Fig. 5) is fully indicative of a transition from collapsed hairpins to a completely folded form.

There are two types of unimolecular antiparallel topography: the "chair" with all three loops in lateral positions and the "basket" topology with the loops positioned in a lateral–diagonal–lateral arrangement (Fig. 1). Since $Na^+$-induced folding of Tel22 to the antiparallel basket topology is also kinetically complex, we suggest that the antiparallel structure of $I_2$ is probably the chair form. Folding into the chair conformation would require only a simple bending from a U-shaped hairpin into the antiparallel structure (Figs. 1a and 12), which could take place in a single step. It is noteworthy that photocrosslinking studies of Su *et al.* provide direct evidence for the presence of chair, basket, and/or triple-helical structures for Tel22 in $K^+$ solutions [46].

### *The $I_2$-to-$I_3$ step: Slow formation of triple-helix intermediate?*

Slow CD changes are observed following the formation of the antiparallel intermediate (Fig. 3). At least two relaxation times are required to account for these slow CD changes. For consecutive first-order reactions, there are always two alternative sets of parameters that can fit the data with identical precision such that the fast and slow kinetic steps are interchanged [75]. A choice between the alternative parameters can be made based on the spectral properties of intermediate species [62]. For the data in Fig. 3, if the slow step is assumed to occur first, a spectrum for the $I_3$ species with enhanced CD at 260 nm may be calculated (Fig. 3b). Such a spectral property was observed in thermal denaturation experiments of Tel22 and was assigned to a triple-helical intermediate species [50]. Assuming that the $I_2$-to-$I_3$ step represents a slow chair-to-triplex transition would be consistent with thermal denaturation studies that proposed such an intermediate [49,50]. Since the triple-helix species is never in high abundance over the time of the reaction (Fig. 3a, middle panel), dramatic changes in CD at 260 nm are not evident in the primary data but can only be inferred by complete analysis of the multidimensional kinetic data. The relaxation time for the $I_2$-to-$I_3$ conversion is about 3700 s.

Additional evidence for the proposed triple-helical intermediate comes from studies of the temperature dependence of the folding rates (Fig. 4b). Thermal denaturation studies of Tel22 showed that, at 55 °C, the most populated species is an intermediate with the CD spectral properties assigned to a triple-helical form [50]. Additional unfolded and quadruplex species are

also present under those conditions in lesser abundance. Kinetic studies conducted at 55 °C show a final CD spectrum identical in shape with that observed for the intermediate in the thermal denaturation experiments (Fig. 4b). This spectrum suggests that $I_3$ is a triple helix and that the kinetic folding pathway we infer is consistent with the thermodynamic denaturation mechanism we described for Tel22 [50].

In addition to the spectroscopic evidence cited above supporting the assignment of an antiparallel chair structure to $I_2$ and a triplex structure to $I_3$, the studies of Su *et al.* provide direct chemical evidence for the coexistence of chair forms and triplex forms for Tel22 in 150 mM KCl at 4 °C [46]. In these studies, the authors identified the sequential positions of thymine photodimers that can only be formed when proximate thymine residues are excited by UV irradiation. Because the loop topography of different antiparallel and hybrid structures differs, a unique pattern of thymine dimer photoproducts is expected for each folding pattern. In particular, crosslinks that could only form between loops 1 and 3 were identified in significant concentration. From these results, the authors proposed an equilibrium involving a triplex intermediate in the interconversion of chair, basket, and hybrid topologies. These results are also consistent with NMR studies suggesting the presence of interconvertible quadruplex topologies [14,39,42].

The molecular driving forces for the proposed chair to triplex formation are not clear. The activation energy for the formation of $I_3$ is estimated to be 22 kcal/mol (Fig. 4c). This value represents a substantial kinetic barrier and explains the slow formation of the triple helix from the proposed antiparallel chair form. Structurally, the transition requires that one arm of the quadruplex breaks one set of hydrogen bonds within the quartet stack and dissociates, freeing it to rearrange to change polarity and to change from a lateral to a side ("chain reversal") loop. The high activation energy indicates that this is an improbable event. The process is perhaps analogous to DNA hairpin opening that has an activation energy of +14 kcal/mol to 32 kcal/mol [76,77], in the same range as the 22 kcal/mol we observe. Mashimo *et al.* computed that the stabilization energy of the G-triplet is similar to that of the G-tetrad, which supports the possibility of a triplex intermediate [45]. Our results show that, while they may be thermodynamically similar, a large kinetic barrier separates the two forms. Further elucidation of the driving forces for this step will require a detailed study of the cation concentration dependency of the rate constants, studies that are beyond the scope of the present study.

### *The $I_3$-to-F step: Formation of final hybrid forms*

The conversion of $I_3$ to the folded hybrid form is the final step, with a relaxation time of about 750 s. We envision this step to be the reassociation and rearrangement of the free arm in $I_3$ to the hybrid conformation with the formation of a side ("chain reversal") loop. This unimolecular process might be rate limited by necessary *syn*-to-*anti* conversions of the nucleotides in the arm prior to reassociation [47]. An activation energy of 26 kcal/mol is associated with this step, indicative of a substantial kinetic barrier. For hairpin closing (perhaps analogous to the proposed $I_3$-to-F step), activation energies have small positive or even negative values [76,77], which makes our observed value surprising and which suggests that another process is at work. The *syn*-to-*anti* transition of a single glycosidic bond is reported to be +6.3 kcal/mol [78]. Thus, as we propose, coupling to the strand closing to form the final folded form to changes in only a few glycosidic bonds could account to the observed 26 kcal/mol. Again, the exact driving forces of this step are not clear but surely involve coupled cation binding steps that need to be characterized by additional study.

### Modeling the $I_2$ to final hybrid forms, observing a triplex intermediate

To determine if there was a stereochemically feasible route from the proposed $I_2$ forms to the final hybrid forms, we used simulated annealing molecular dynamics simulations using the nudged elastic band method to construct a pathway. This involved setting the two endpoints of the simulations and locating a low-energy pathway between them. The two chair forms of Tel22 and the 22mer truncated forms of the NMR structures for hybrid-1 (2HY9) and hybrid-2 (2JPZ) were used as the endpoints (Fig. 13). The simulation was not an extensive survey of the energy surface and low-energy pathways but rather was used to provide one possible pathway. This method has not been previously applied to quadruplex system and provides new insights into their folding pathway.

The simulations were able to successfully map a pathway from the $I_2$ to the hybrid forms with the disruption of the 5′ or 3′ run of three guanine Hoogsten hydrogen bonds for the chair forms, forming triplex intermediates. After the rotation of the guanine bases around the glycosidic bonds to the appropriate conformation, the Hoogsten hydrogen bonds reformed with the double chain reversal loop, thus replacing the lateral loop. Under the restraints of the nudged elastic band conditions, the 5′ or 3′ run of three guanines that break hydrogen bonds to form the resulting triplex does not need to be completely disassociated from the triplex during the refolding process to the hybrid forms. It is interesting to note that the central potassium ions are mobile and one transiently leaves the double guanine triplet stack O6 coordination during the simulation (Fig. 13b).

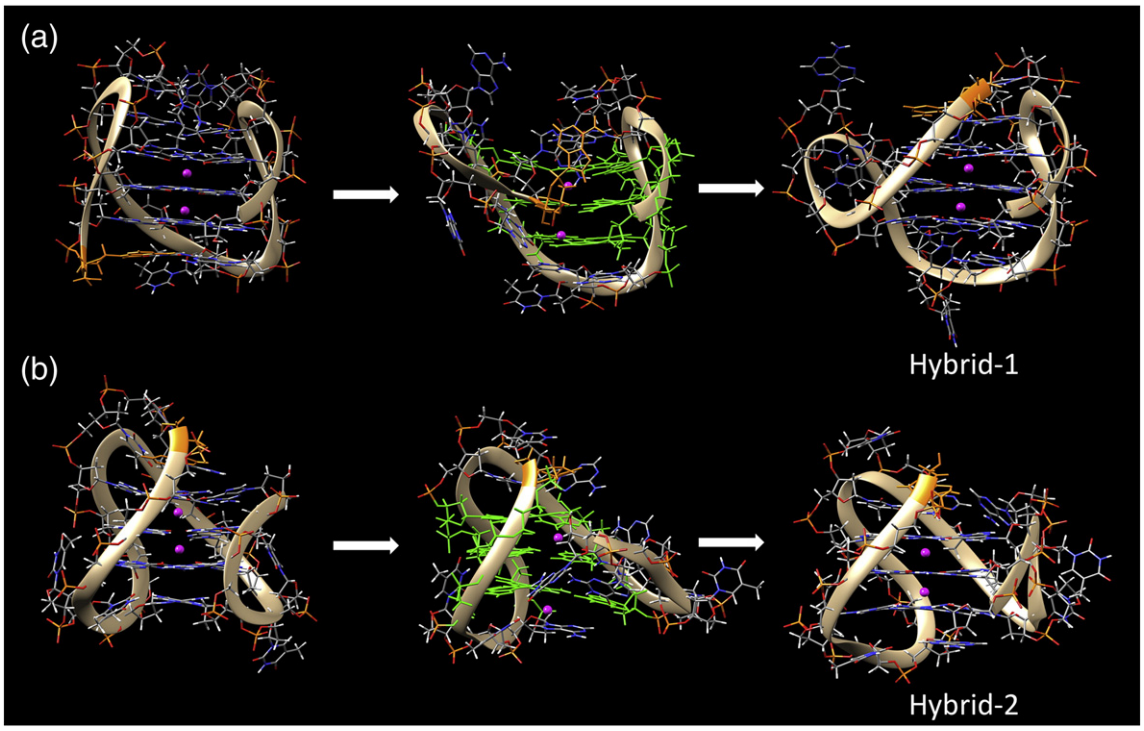


**Fig. 13.** Modeling the $I_2$ to hybrid form 1 and 2 pathways. Hybrid-1 (a) and hybrid-2 (b) forming through a triplex intermediate from the corresponding chair form. The conserved triplex bases are shown in green and potassium ions are in magenta ball representation. The 5′-A base is colored orange for orientation. An animated version of the pathway is provided in Supplemental Data.

## Comparison of folding kinetics by different spectroscopic probes

Figure 8 shows a comparison of folding kinetics assessed by different probes and summarizes a large number of kinetic experiments. The figure is a composite representation of the relative signal change *versus* logarithmic time for folding for Tel22 detected by 2-AP fluorescence, FRET, or CD at two different potassium concentrations. Based on the sizes of the signal changes, the kinetic profiles appear to be divisible into four time frames corresponding roughly to the time constants for the four phases detected in these experiments: $<10^{-2}$ s, $10^{-2}$ to 1 s, 10 to $10^2$ s, and $10^2$ to $10^4$ s. For the $<10^{-2}$ s segment, only the FRET signals (middle panel) show a rapid change. As pointed out above, this could reflect formation of hairpins from the "unfolded" ensemble and would therefore describe the formation of $I_1$ in Scheme 1.

During the $10^{-2}$ to 1 s time period, the signals associated with AP7, AP19, AP13, 520-nm FRET, and CD change more or less in unison during time interval while AP1 fluorescence remains practically constant. The rate of change of these signals depends on $[K^+]$ as expected from our previous study where folding was monitored by UV absorption spectroscopy. A major fraction of the CD change at 285 nm and 260 nm occurs in this period. Taken together, these results are consistent with a $[K^+]$-dependent step that results in formation of stacked G-quartets and may be identified with $I_2$, which we propose to be an antiparallel quadruplex. Since the AP1 signal does not change during this period, it probably does not participate directly in this step.

The 1 to $10^2$ s time period shows little or no change in CD signal but substantial changes in FRET efficiency and changes in the emission of AP1, AP7, and AP19. These changes are weakly dependent on $[K^+]$. The lack of change in CD signal but changes in 2AP fluorescence and FRET efficiency suggest conversion of the antiparallel structure to $I_3$, perhaps a triplex structure. Finally, during the $10^2$ to $10^4$ time segment, the rearrangement process is completed with formation of the final equilibrium distribution of hybrid-1 and hybrid-2 structures. This stage of the reaction is characterized by significant changes in AP1, AP7, and AP19 fluorescence emission, as well as changes in FRET and CD signal.

### Comparison of the kinetics of folding with the kinetics of conformational switching induced by $Na^+ \rightarrow K^+$ exchange

Our previous kinetic study [60] of the conversion of the $Na^+$-basket form to the $K^+$-hybrid form is consistent with our interpretation of the current folding experiments. In these studies, Tel22 in 30 mM NaCl was mixed with KCl to give a final [$K^+$] of 50 mM, which is sufficient to completely convert the basket in $Na^+$ to a mixture of hybrid-1 and hybrid-2 forms. Previous investigators have shown that replacement of $Na^+$ by $K^+$ within the quadruplex channel is completed within ~250 μs [29,79,80]. Using manual mixing (dead time of 5–7 s) and wavelength scanning CD spectroscopy, we found a triphasic time course with the most rapid CD change taking place during the mixing time followed by two-exponential steps with time constants of ~50 s and ~800 s. The initial rapid step no doubt corresponds to displacement of $Na^+$ by $K^+$. We suggested that the CD spectrum of the first intermediate as determined by SVD analysis is that of the potassium-loaded basket form of Tel22; with a peak at ~290 nm and a trough at ~260 nm, this intermediate spectrum resembles that of the 1-s folding intermediate in Fig. 3a. The rapidly formed $K^+$-basket was proposed to relax in a two-step process in which the $\tau_1 = 50$ s step is formation of a mixture of triplexes while the $\tau_2 = 800$ s step represents a rearrangement to the final mixture of conformers. In light of the current studies, we re-fit the previous Na-to-K exchange data set to a two-exponential relaxation with the requirement $\tau_1 > \tau_2$. SVD fitting produced a calculated intermediate CD spectrum with a maximum at ~265 nm, the signature wavelength of the triplex. These kinetics are similar to the triphasic kinetics of Tel22 folding in Figs. 5 and 6, in which three relaxations were observed with time constants of 1 s, 600 s, and 3000 s.

### Unfolding

The kinetics of biopolymer unfolding also provides information that can be related to mechanism, as well as provides insight into biological function in regulatory situations requiring switching between folded and unfolded states or between conformational states. Quadruplex unfolding kinetics can be assessed using a number of experimental approaches. One method that has been applied involves mixing the pre-formed quadruplex with an excess of its DNA complement [81,82]. In the presence of complementary DNA, partially unfolded species formed as a result of thermal motion will be trapped as a stable duplex resulting eventually in complete unfolding of the quadruplex as more of the folded structure shifts to the duplex. Duplex formation has been shown not to be rate limiting; thus, the rate of unfolding can be assessed as an irreversible reaction. Since the spectroscopic properties of the quadruplex and duplex are generally distinct from one another, one can easily track the progress of unfolding.

In the current experiments, the unfolding kinetics of Tel22, 2AP-Tel22, 2GKU, and 2JSL were multiphasic in all of the experiments in which Tel22-comp was used as the trapping agent. Generally, two relaxations times of 300–600 s and 4800–15,600 s were observed. These values are similar to the values of ~300 s and ~3000 s found by Lane in NMR-detected unfolding experiments involving Tel22 and its complement in 25 mm KCl [81]. It is important to note that 2GKU and 2JSL, which are homogeneous hybrid-1 and hybrid-2 forms, respectively, also exhibit multiphasic unfolding kinetics (Fig S11). This implies that the observed kinetic complexity in unfolding results from the presence of structural intermediates along a sequential unfolding pathway rather than from parallel unfolding reaction due to structural heterogeneity in the starting material. It is interesting that the hybrid-1 and hybrid-2 topologies have about the same time constant for the fast step (360 s and 40 s), but the slower step is about half as fast for 2GKU as for 2JSL (15,780 s and 7020 s, respectively). If Tel22 consisted of an equimolar mixture of hybrid-1 and hybrid-2 that unfold independently, we would expect triphasic unfolding kinetics with two discernible slow phases reflecting the different slow rates of unfolding of the two different conformers. This observed slow phase of unfolding for Tel22 ($\tau = 5100$ s) is inconsistent with the hypothesis that the kinetic heterogeneity results from pre-existing conformational heterogeneity and supports the notion that kinetic heterogeneity results from the presence of intermediates with different kinetic properties. In this regard, it is relevant that Ying *et al.* found conformational heterogeneity for an analog of the human telomeric repeat d[$(GGGTTA)_3GGG$] attached to a 35-residue duplex in the presence of either $Na^+$ or $K^+$ [54]. However, in similar complement trapping experiments, both conformers unfolded at the approximately the same rate of ($\tau \approx 780$ s).

## Conclusions

DNA has not generally been associated with formation of compact, folded structures. However, over the past decade as many quadruplex structures have been determined by X-ray crystallography and high-resolution NMR, it has become clear that, under appropriate conditions, G-rich oligodeoxynucleotides can in fact fold into globular structures characterized by quartets of stacked, hydrogen-bonded G residues surrounded by connecting loops that can adopt various topological arrangements. The equilibrium ensemble of topologies depends on DNA sequence, solution conditions, cation size, and temperature. Most, if not

**Table 1.** Oligonucleotides used in this study

| Oligonucleotide name | Sequence | $\varepsilon_{mM}$ (260 nm) |
|---|---|---|
| Tel22 | d[AGGG(TTAGGG)$_3$] | 228.5 |
| Tel22-comp | d[CCC(TAACCC)$_3$ T] | 193.7 |
| 2GKU[1] | d[TTGGG(TTAGGG)$_3$A] | 244.3 |
| 2JSL[1] | d[TAGGG(TTAGGG)$_3$TT] | 253.1 |
| 6-Fam-Tel22-Tamra | 6-Fam and Tamra attached | 228.5 |
| 6-Fam-2GKU-Tamra | through 6-carbon linkers to 5′ | 193.7 |
| 6-Fam-2JSL-Tamra | and 3′ ends of the parent DNA sequences | 244.3 |

[1] PDB accession code for the NMR-derived structure in $K^+$.

all, of the quadruplex-dependent biological processes outlined in the introduction depend on folding–unfolding cycles, as well as presentation of specific surface features to DNA, RNA, or protein binding partners. Thus, the pathways that a quadruplex DNA sequence follows in folding into these complex topological arrangements are of fundamental importance for understanding their biological function.

The current study demonstrates that DNA quadruplexes fold into compact structures by following a multistep pathway that involves a cation-induced collapse of the unfolded ensemble of chains into an ensemble of hairpin structures. The hairpins collapse further into an ensemble of antiparallel structures, possibly chair-type structures. The structure of the remaining intermediate is probably an ensemble of triplex states. This is supported by the unfolding experiments implying that the first step of unfolding is likely to proceed through a triplex. Thus, the folding mechanism for quadruplexes includes aspects of both of the Mashimo [44,45] mechanisms: antiparallel chairs and triplexes.

## Materials and Methods

### Materials

The sequence of oligonucleotides, their abbreviations, and their calculated extinction coefficients are given in Table 1. The oligonucleotides were obtained from Integrated DNA Technologies (Coralville, IA) in the form of desalted, lyophilized products. Fluorescent oligonucleotides for FRET analysis were HPLC purified and were obtained from Sigma, St. Louis, MO. These oligonucleotides contained a 6-Fam donor linked through a 6-carbon tether at the 5′ end and a Tamra acceptor moiety linked by a 6-carbon tether to the 3′ end. Oligonucleotides Tel22, 2GKU, and 2JSL were dissolved in folding buffer (10 mM tetrabutylammonium phosphate, 1 mM ethylenediaminetetraacetic acid, pH 7.0) at a strand concentration of ~1 mM and stored at 4 °C. The fluorescently labeled oligonucleotides were dissolved in folding buffer at a concentration of ~250 μM. To ensure that unfolded oligonucleotides were in a disaggregated, unfolded state prior to $K^+$-jump kinetic experiments, we heated them to ~90 °C in a water bath for ~10 min and slowly cooled them overnight to room temperature. Oligonucleotides for unfolding kinetic experiments were also heated to 90 °C in the presence of the desired concentration of KCl for ~10 min and then slowly cooled overnight to room temperature. The oligonucleotide Tel22-comp was preheated to 50 °C prior to adding to the folded oligonucleotide to initiate unfolding kinetic experiments. Oligonucleotide concentrations were calculated from the 260-nm absorbance of the $K^+$-free solutions using the absorption coefficients in Table 1.

Tetrabutylammonium phosphate, tetrabutylammonium hydroxide (40% aqueous solution), KCl, and ethylenediaminetetraacetic acid (acid form) were from Sigma Chemical Co. (St. Louis, MO).

### Methods

#### *CD spectroscopy*

The rapid kinetics of quadruplex folding was measured using a Jasco J-810 CD spectrophotometer equipped with a Jasco SF-492 stopped-flow mixing device (Jasco, Easton, MD). Heat-denatured, unfolded oligonucleotide at a concentration of 45–55 μM was mixed with 20 or 50 mM KCl in folding buffer. Generally, five to eight reaction records were collected and averaged to produce a kinetic time course over the desired time range (1 s to $10^4$ s). The observation path length of the CD cell was 0.2 cm, the reaction volume was 150 μL, and the reagents were at room temperature (~22.5 °C). Other instrumental parameters were as follows: flow time, 15 ms; 75 μL of each reactant; spectral bandwidth, 5 nm; digital integration time, 0.5 ms to 2 s, depending on the rate of data collection. Data collection was initiated 75 ms before flow stopped so that the initial signal observed is that of the aged reaction mixture followed by replacement of the solution from the previous run with freshly mixed reagents. For the kinetic spectra, individual reactions were monitored at 5-nm intervals over the wavelength range 240–305 nm in separate experiments. Control experiments indicated that data collected 80–90 ms after mixing were reliable. The CD and absorbance spectra of the $K^+$-free oligonucleotide was scanned after mixing DNA with buffer; the spectra of the folded sample was obtained at the conclusion of the kinetic run. Blank spectra obtained after mixing buffer with buffer were subtracted from the DNA spectra. Where indicated, the observed ellipticity θ in millidegrees was normalized using the expression $\Delta\varepsilon = \theta/(32{,}980 \times c \times l)$, where $c$ is the molar strand concentration and $l$ is the path length in centimeters. Kinetic constants and signal amplitudes were obtained by fitting the θ *versus* time data sets at a particular wavelength by nonlinear least squares to an appropriate exponential expression (see Data analysis below) using routines in either Origin 7.0 or GraphPad Prism.

The slower phases of the folding or unfolding reactions could be more conveniently obtained in manual mixing experiments. For these experiments, folding was initiated by rapidly (5–7 s) mixing either an aliquot of 3 M KCl with heat-denatured oligonucleotide (4–6 μM) or 1 mM complement DNA with the folded oligonucleotide in a 1-cm path length cuvette equipped with magnetic stirring. An initial CD spectrum of the unfolded (or folded) oligonucleotide was recorded after which either KCl or the DNA complement was

added. Successive CD spectra were determined over the wavelength range 320–220 nm after mixing for up to $10^4$ s. Instrumental parameters were as follows: scanning rate, 200 nm/min; spectral bandwidth, 1 nm; resolution, 1 nm; digital integration time, 2 ms. The sample was maintained at 25 ºC with a Peltier controller.

### *Fluorescence and rapid scanning UV stopped-flow kinetics*

An OLIS RSM stopped-flow system (On-Line Instrument Systems, Bogart, GA) equipped with a 75-W Xe lamp was used to monitor folding of the fluorescent labeled and unlabeled oligonucleotides over the time range 1 s to $10^4$ s. In its rapid scanning absorbance mode, the instrument was used essentially as previously described to record time-dependent changes in UV absorbance as a function of wavelength [57]. The data collection program produces a data matrix consisting of rows of absorbance values at a series of wavelengths between 270 and 320 nm and columns of absorbance at each wavelength *versus* time. The resulting multidimensional data sets were analyzed by SVD and the results fit to an appropriate mechanism by nonlinear least squares using software supplied by OLIS (GlobalWorks).

The same instrument was also used in a fluorescence configuration to record changes in 2-AP, 6-Fam, or Tamra fluorescence. 2-AP labeled oligonucleotides were excited at 305 nm and emission was detected at 90º to excitation through a 320-nm-cutoff filter (1-CGA-320). For the FRET oligonucleotides, the 6-Fam donor was excited at 490 nm and its emission was detected through an interference filter centered at 520 nm (10BPF10-520). Optical filters were purchased from Newport Corp., Franklin, MA. The reactions were maintained at 25 ºC with a circulating water bath.

### *Manual mixing fluorescence kinetics*

Manual mixing of reactants was used for determining the kinetics of the relatively slow quadruplex unfolding reactions. Duplex trapping was initiated by rapidly adding a 5-fold excess of 1 mM complementary DNA to a stirred solution of annealed oligonucleotide in either 25 mM KCl. The complement forms a stable duplex with single-stranded, partially unfolded segments of the quadruplex produced by thermal motion. Duplex formation is rapid and therefore not rate limiting in these experiments.

A FluoroMax-3 spectrofluorometer (Horiba, Edison, NJ) equipped with an in-cell magnetic stirrer and a thermostated cell holder maintained at 25 ºC was used for the duplex trapping experiments involving fluorescent quadruplexes. A 1-nm excitation slit and a 5-nm emission slit were used for all experiments. Oligonucleotides containing 2-AP were excited at 305 nm and emission spectra were measured at 1-nm intervals from 310 to 450 nm. Single-wavelength kinetics was followed at the emission maximum of 320 nm. Kinetic constants and signal amplitudes were determined by nonlinear least squares as described below.

For the unfolding kinetics of FRET-labeled oligonucleotides, the FluoroMax instrument was programmed to scan the emission spectrum from 500 to 603 nm at 30-s intervals. Excitation was at 490 nm. After collecting a baseline (folded) emission spectrum, an aliquot of 1 mM Tel22 complement DNA was added to the folded FRET oligonucleotide at ~ 1 μM concentration in 25 mm KCl. The resulting $F(\lambda)$ *versus* time data matrix was analyzed by SVD and fit to an appropriate exponential expression as described below.

### *Fluorescence lifetime measurements*

Fluorescence lifetimes were determined at room temperature using an ISS K2 Multifrequency Phase Fluorometer (Champaign, IL) equipped with a 468-nm LED excitation source and a 520-nm band pass filter for emission measurements (Newport Corp.). Sample volume was 1.0 ml in a 1-cm cuvette. Phase and amplitude modulation data sets were analyzed using the program Vinci Beta 1.7 (ISS). The instrument was calibrated with fluorescein in 0.1 M NaOH ($\tau$ = 4.0 ns).

### *Molecular modeling*

The $I_2$ transitions to hybrid forms 1 and 2 were modeled by the nudged elastic band method as implemented in the AMBER 12 program [83]. The two Tel22 $I_2$ antiparallel chair structures (Fig. 12), precursors to hybrid-1 and hybrid-2, were created by Quadgen [84], a program that produces all possible two- and three-dimensional quadruplex forms for any given sequence, using first known stems and loops, and then modeled sequences. The initial models were explicitly solvated and potassium counterions were generated with the parm12SB.dat AMBER force field using the following protocol: (i) two unsolvated potassium ions were placed between the G-quartet tetrads for stabilization, (ii) the system was solvated by the addition of a rectangular box of TIP3P water at 15 Å, and (iii) neutralizing solvated potassium ions were added randomly around the quadruplex structures using AMBER 12 leap rules for counterions. Energetically stable models were generated using the following protocol: minimize water holding the DNA (50 kcal $mol^{-1}$ $Å^{-1}$), minimize the complete system, 50-ps molecular dynamics (heating to 300 K) holding the DNA fixed (50 kcal $mol^{-1}$ $Å^{-1}$), (iv) unrestrained molecular dynamics for 10 ns. Simulations were performed in the isothermal isobaric ensemble ($P$ = 1 atm; $T$ = 300 K). Periodic boundary conditions and the Particle-Mesh-Ewald algorithm were used. A 2.0-fs time step was used with bonds involving hydrogen atoms frozen using SHAKE. For the equilibration steps and the production steps, molecular dynamics calculations were carried out using AMBER 12 program sander and the cuda version of pmemd, respectively. The final preparation step was minimization with implicit solvent, igb = 1 and saltcon = 0.2. The hybrid-1 and hybrid-2 forms were truncated from 2HY9 and 2JPZ to the Tel22 sequence and minimized with implicit solvent, igb = 1 and saltcon = 0.2.

The nudged elastic band method using simulated annealing was used to map a pathway from $I_2$ to the hybrid form using multisander as per the AMBER website [85], 192 images were used, and tgtfitmask = ":1-24" including the tetrad core potassium ions and tgtrmsmask = ":1-22@P,O1P,O2P,O5′,O3′" were used. The endpoints were set as the chair and corresponding hybrid form. The five steps were (i) heating: linear heating from 0 to 300 K for 20 ps with a 0.5 fs time step with neb options skmin = 10,skmax = 10; (ii) equilibrium: 300 K 100 ps with a 1 fs time step with skmin = 50,skmax = 50 used and in subsequent steps; (iii) simulated annealing:

600 ps, 1 fs time step, 0–50 ps heat 300–400 K, 50–100 ps 400 K, 100–150 ps heat 400–500 K, 150–200 ps 500 K, 200–250 ps cool to 300 K, 250–300 ps 300 K; (iv) slow cooling: 120 ps with 1 fs time step 300–0 K; (v) long cool: 200 ps 0 K with skmin = 10,skmax = 10. The final pathway was extracted and visualized using a modified combine_final_pathway.sh script (Fig. 13 and Supplementary Movies 1 and 2).

### Data analysis

Single-wavelength kinetic curves were analyzed by fitting the data points to a sum of exponentials that include a zero-order background component:

$$S_t = S_\infty + \sum \Delta S_i \cdot exp(-t/\tau_i) + S_{i+1} \cdot t \quad (1)$$

where $S_t$ is the signal at time $t$, $S_\infty$ is the magnitude of the signal at the completion of the reaction, $\Delta S_i$ is the change in signal amplitude associated with component $i$, and $\tau_i$ is the time constant for step $i$. The term $S_{i+1} \cdot t$ was used only in the analysis of FRET data to account for a small amount of zero-order photolysis of the 6-Fam moiety. Values of $S_\infty$, $S_i$, and $\tau_i$ were adjusted to minimize the sum of squared residuals using nonlinear least-squares routines in either Origin 7.0 (OriginLab Corp., Northampton, MA) or Prism 4.0 (GraphPad Software, La Jolla, CA). The observed experimental time courses often consisted of the sum of two or three exponential relaxations [i.e., $i = 2$ or 3 in Eq. (1)]. With multi-exponential data, least-squares fitting is ambiguous with respect to the relative order of the relaxation times (e.g., in the two-step reaction A → B → C, equally good fits are returned with $\tau_1 > \tau_2$ or $\tau_2 > \tau_1$) [62]. However, the amplitude of the signal change for the individual steps depends on whether the first or second step is faster. Thus, additional information (such as spectroscopic or chemical information) is required to resolve the ambiguity in assignment of the rate-limiting step [63].

Multiwavelength kinetic data were organized into data matrices consisting of rows of signal amplitudes *versus* time and columns of signal amplitudes *versus* wavelength. These data matrices were analyzed using the SVD and nonlinear least-squares fitting routines in the program GlobalWorks (OLIS, Bogart, GA). This software performs SVD analysis of three-dimensional data sets and has provisions for fitting fits kinetic eigenvectors to a mathematical expression describing a chosen mechanism. The program outputs the best-fitting kinetic constants, their standard deviations, a comparison of the calculated and experimental eigenvectors, a residual plot, the absolute spectra of the kinetically significant species, and a time profile for each of the spectroscopically significant species.

Supplementary data to this article can be found online at http://dx.doi.org/10.1016/j.jmb.2014.01.009.

## Acknowledgements

This study is supported by grant CA35635 from the National Cancer Institute and by grant GM077422 from the National Institutes of Health.

*Received 6 November 2013;*
*Received in revised form 6 January 2014;*
*Accepted 7 January 2014*
Available online 31 January 2014

***Keywords:***
kinetics;
stopped-flow;
folding intermediates;
triplex;
circular dichroism



***Abbreviations used:***
2-AP, 2-aminopurine; FRET, fluorescence resonance energy transfer; 6-Fam, 6-carboxyfluorescein; Tamra, 5-carboxytetramethylrhodamine; SVD, singular value decomposition.

## References

[1] Leventhal C. How to fold graciously. In: Debrunner P, Tsibris JCM, Munck E, editors. Mossbauer spectroscopy in biological systems: proceedings of a meeting held at Allerton House. Monticello, Illinois: University of Illinois Press; 1969. p. 22–4.
[2] Thirumalai D, Hyeon C. RNA and protein folding: common themes and variations. Biochemistry 2005;44:4957–70.
[3] Spatz HC, Crothers DM. The rate of DNA unwinding. J Mol Biol 1969;42:191–219.
[4] Wetmur JG, Davidson N. Kinetics of renaturation of DNA. J Mol Biol 1968;31:349–70.
[5] Ansari A, Kuznetsov SV. Is hairpin formation in single-stranded polynucleotide diffusion-controlled? J Phys Chem B 2005;109:12982–9.
[6] Ansari A, Kuznetsov SV, Shen Y. Configurational diffusion down a folding funnel describes the dynamics of DNA hairpins. Proc Natl Acad Sci U S A 2001;98:7771–6.
[7] Kuznetsov SV, Ansari A. A kinetic zipper model with intrachain interactions applied to nucleic acid hairpin folding kinetics. Biophys J 2012;102:101–11.
[8] Narayanan R, Zhu L, Velmurugu Y, Roca J, Kuznetsov SV, Prehna G, et al. Exploring the energy landscape of nucleic acid hairpins using laser temperature-jump and microfluidic mixing. J Am Chem Soc 2012;134:18952–63.
[9] Nayak RK, Peersen OB, Hall KB, Van Orden A. Millisecond time-scale folding and unfolding of DNA hairpins using rapid-mixing stopped-flow kinetics. J Am Chem Soc 2012;134:2453–6.
[10] Yin Y, Wang P, Yang XX, Li X, He C, Zhao XS. Panorama of DNA hairpin folding observed via diffusion-decelerated fluorescence correlation spectroscopy. Chem Commun 2012;48:7413–5.
[11] Yin Y, Zhao XS. Kinetics and dynamics of DNA hybridization. Acc Chem Res 2011;44:1172–81.
[12] Keniry MA. Quadruplex structures in nucleic acids. Biopolymers 2000;56:123–46.
[13] Davis JT. G-Quartets 40 years later: from 5′-GMP to molecular biology and supramolecular chemistry. Angew Chem Int Ed 2004;43:668–98.

[14] Dai J, Carver M, Yang D. Polymorphism of human telomeric quadruplex structures. Biochimie 2008;90:1172–83.
[15] De Cian A, Lacroix L, Douarre C, Temime-Smaali N, Trentesaux C, Riou J-F, et al. Targeting telomeres and telomerase. Biochimie 2008;90:131–55.
[16] Lane AN, Chaires JB, Gray RD, Trent JO. Stability and kinetics of G-quadruplex structures. Nucleic Acids Res 2008;36:5482–515.
[17] Shay JW, Wright WE. Role of telomeres and telomerase in cancer. Semin Cancer Biol 2011;21:349–53.
[18] Sen D, Gilbert W. Formation of parallel four-stranded complexes by guanine-rich motifs in DNA and its implications for meiosis. Nature 1988;334:364–6.
[19] Moyzis RK, Buckingham JM, Cram LS, Dani M, Deaven LL, Jones MD, et al. A highly conserved repetitive DNA sequence, $(TTAGGG)_n$, present at the telomeres of human chromosomes. Proc Natl Acad Sci U S A 1988;85:6622–6.
[20] Williamson JR, Raghuraman MK, Cech TR. Monovalent cation-induced structure of telomeric DNA: the G-quartet model. Cell 1989;59:871–80.
[21] O'Sullivan RJ, Karlseder J. Telomeres: protecting chromosomes against genome instability. Nat Rev Mol Cell Biol 2010;11:171–81.
[22] Xu Y. Chemistry in human telomere biology: structure, function and targeting of telomere DNA/RNA. Chem Soc Rev 2011;40:2719–40.
[23] Bochman ML, Paeschke K, Zakian VA. DNA secondary structures: stability and function of G-quadruplex structures. Nat Rev Genet 2012;13:770–80.
[24] Schaffitzel C, Berger I, Postberg J, Hanes J, Lipps HJ, Pluckthun A. *In vitro* generated antibodies specific for telomeric guanine-quadruplex DNA react with *Stylonychia lemnae* macronuclei. Proc Natl Acad Sci U S A 2001;98:8572–7.
[25] Hänsel R, Löhr F, Trantirek L, Dötsch V. High-resolution insight into G-overhang architecture. J Am Chem Soc 2013;135:2816–24.
[26] Biffi G, Tannahill D, McCafferty J, Balasubramanian S. Quantitative visualization of DNA G-quadruplex structures in human cells. Nat Chem 2013;5:182–6.
[27] Granotier C, Pennarun G, Riou L, Hoffschir F, Gauthier LR, De Cian A, et al. Preferential binding of a G-quadruplex ligand to human chromosome ends. Nucleic Acids Res 2005;33:4182–90.
[28] Gellert M, Lipsett MN, Davies DR. Helix formation by guanylic acid. Proc Natl Acad Sci U S A 1962;48:2013–8.
[29] Hud NV, Plavec J. The role of cations in determining quadruplex structure and stability. In: Neidle SB, Balasubramanian S, editors. Quadruplex nucleic acids. Cambridge, UK: RSC Publishing; 2006.
[30] Neidle S. The structures of quadruplex nucleic acids and their drug complexes. Curr Opin Struct Biol 2009;19:239–50.
[31] Yang D, Okamoto K. Structural insights into G-quadruplexes: towards new anticancer drugs. Future Med Chem 2010;2:619–46.
[32] Collie GW, Parkinson GN. The application of DNA and RNA G-quadruplexes to therapeutic medicines. Chem Soc Rev 2011;40:5867–92.
[33] Wang Y, Patel DJ. Solution structure of the human telomeric repeat $d[AG_3(T_2AG_3)_3]$ G-tetraplex. Structure 1993;1:263–82.
[34] Parkinson GN, Lee MP, Neidle S. Crystal structure of parallel quadruplexes from human telomeric DNA. Nature 2002;417:876–80.
[35] Miller MC, Buscaglia R, Chaires JB, Lane AN, Trent JO. Hydration is a major determinant of the G-quadruplex stability and conformation of the human telomere 3′ sequence of d $[AG_3(TTAG_3)_3]$. J Am Chem Soc 2010;132:17105–7.
[36] Buscaglia R, Miller MC, Dean WL, Gray RD, Lane AN, Trent JO, et al. Polyethylene glycol binding alters human telomere G-quadruplex structure by conformational selection. Nucleic Acids Res 2013;41:7934–46.
[37] Li J, Correia JJ, Wang L, Trent JO, Chaires JB. Not so crystal clear: the structure of the human telomere G-quadruplex in solution differs from that present in a crystal. Nucleic Acids Res 2005;33:4649–59.
[38] Hänsel R, Löhr F, Foldynová-Trantírková S, Bamberg E, Trantírek L, Dötsch V. The parallel G-quadruplex structure of vertebrate telomeric repeat sequences is not the preferred folding topology under physiological conditions. Nucleic Acids Res 2011;39:5768–75.
[39] Ambrus A, Chen D, Dai J, Bialis T, Jones RA, Yang D. Human telomeric sequence forms a hybrid-type intramolecular G-quadruplex structure with mixed parallel/antiparallel strands in potassium solution. Nucleic Acids Res 2006;34:2723–35.
[40] Phan AT, Luu KN, Patel DJ. Different loop arrangements of intramolecular human telomeric (3 + 1) G-quadruplexes in $K^+$ solution. Nucleic Acids Res 2006;34:5715–9.
[41] Luu KN, Phan AT, Kuryavyi V, Lacroix L, Patel DJ. Structure of the human telomere in $K^+$ solution: an intramolecular (3 + 1) G-quadruplex scaffold. J Am Chem Soc 2006;128:9963–70.
[42] Xu Y, Noguchi Y, Sugiyama H. The new models of the human telomere $d[AGGG(TTAGGG)_3]$ in $K^+$ solution. Bioorg Med Chem 2006;14:5584–91.
[43] Phan AT, Kuryavyi V, Luu KN, Patel DJ. Structure of two intramolecular G-quadruplexes formed by natural human telomere sequences in $K^+$ solution. Nucleic Acids Res 2007;35:6517–25.
[44] Mashimo T, Sugiyama H. Folding pathways of human telomeric hybrid G-quadruplex structure. Nucleic Acids Symp Ser 2007;51:239–40.
[45] Mashimo T, Yagi H, Sannohe Y, Rajendran A, Sugiyama H. Folding pathways of human telomeric type-1 and type-2 G-quadruplex structures. J Am Chem Soc 2010;132:14910–8.
[46] Su DG, Fang H, Gross ML, Taylor JS. Photocrosslinking of human telomeric G-quadruplex loops by anti cyclobutane thymine dimer formation. Proc Natl Acad Sci U S A 2009;106:12861–6.
[47] Stadlbauer P, Krepl M, Cheatham III TE, Koca J, Sponer J. Structural dynamics of possible late-stage intermediates in folding of quadruplex DNA studied by molecular simulations. Nucleic Acids Res 2013;41:7128–43.
[48] Koirala D, Mashimo T, Sannohe Y, Yu Z, Mao H, Sugiyama H. Intramolecular folding in three tandem guanine repeats of human telomeric DNA. Chem Commun 2012;48:2006–8.
[49] Boncina M, Lah J, Prislan I, Vesnaver G. Energetic basis of human telomeric DNA folding into G-quadruplex structures. J Am Chem Soc 2012;134:9657–63.
[50] Gray RD, Buscaglia R, Chaires JB. Populated intermediates in the thermal unfolding of the human telomeric quadruplex. J Am Chem Soc 2012;134:16834–44.
[51] Buscaglia R, Gray RD, Chaires JB. Thermodynamic characterization of human telomere quadruplex unfolding. Biopolymers 2013;99:1006–18.
[52] An N, Fleming AM, Burrows CJ. Interactions of the human telomere sequence with the nanocavity of the α-hemolysin ion channel reveal structure-dependent electrical signatures for hybrid folds. J Am Chem Soc 2013;135:8562–70.
[53] Lee JY, Okumus B, Kim DS, Ha T. Extreme conformational diversity in human telomeric DNA. Proc Natl Acad Sci U S A 2005;102:18938–43.
[54] Ying L, Green JJ, Li H, Klenerman D, Balasubramanian S. Studies on the structure and dynamics of the human telomeric G quadruplex by single-molecule fluorescence

resonance energy transfer. Proc Natl Acad Sci U S A 2003;100:14629–34.
[55] Ren J, Qu X, Trent JO, Chaires JB. Tiny telomere DNA. Nucleic Acids Res 2002;30:2307–15.
[56] Gaynutdinov TI, Brown P, Neumann RD, Panyutin IG. Duplex formation at the 5′ end affects the quadruplex conformation of the human telomeric repeat overhang in sodium but not in potassium. Biochemistry 2009;48:11169–77.
[57] Gray RD, Chaires JB. Kinetics and mechanism of $K^+$- and $Na^+$-induced folding of models of human telomeric DNA into G-quadruplex structures. Nucleic Acids Res 2008;36:4191–203.
[58] Zhang AY, Balasubramanian S. The kinetics and folding pathways of intramolecular G-quadruplex nucleic acids. J Am Chem Soc 2012;134:19297–308.
[59] Gray RD, Petraccone L, Trent JO, Chaires JB. Characterization of a $K^+$-induced conformational switch in a human telomeric DNA oligonucleotide using 2-aminopurine fluorescence. Biochemistry 2010;49:179–94.
[60] Gray RD, Li J, Chaires JB. Energetics and kinetics of a conformational switch in G-quadruplex DNA. J Phys Chem B 2009;113:2676–83.
[61] Karsisiotis AI, Hessari NM, Novellino E, Spada GP, Randazzo A, Webba da Silva M. Topological characterization of nucleic acid G-quadruplexes by UV absorption and circular dichroism. Angew Chem Int Ed 2011;50:10645–8.
[62] Adcock NWD, Benton DJ, Moore P. Kinetics of series first-order reactions. Analysis of spectrophotometric data by the method of least squares and an ambiguity. Trans Faraday Soc 1970;66:2210–3.
[63] Andraos J. The problem of distinguishability of rate constants in the two-step consecutive sequence A → B → C. Can J Chem 1999;77:565–76.
[64] Edman L, Mets U, Rigler R. Conformational transitions monitored for single molecules in solution. Proc Natl Acad Sci U S A 1996;93:6710–5.
[65] Neubauer H, Gaiko N, Berger S, Schaffer J, Eggeling C, Tuma J, et al. Orientational and dynamical heterogeneity of Rhodamine 6G terminally attached to a DNA helix revealed by NMR and single-molecule fluorescence spectroscopy. J Am Chem Soc 2007;129:12746–55.
[66] Torimura M, Kurata S, Yamada K, Yokomaku T, Kamagata Y, Kanagawa T, et al. Fluorescence-quenching phenomenon by photoinduced electron transfer between a fluorescent dye and a nucleotide base. Anal Sci 2001;17:155–60.
[67] Jean JM, Hall KB. 2-Aminopurine fluorescence quenching and lifetimes: role of base stacking. Proc Natl Acad Sci U S A 2001;98:37–41.
[68] O'Neill MA, Barton JK. 2-Aminopurine: a probe of structural dynamics and charge transfer in DNA and DNA:RNA hybrids. J Am Chem Soc 2002;124:13053–66.
[69] Ballin JD, Bharill S, Fialcowitz-White EJ, Gryczynski I, Gryczynski Z, Wilson GM. Site-specific variations in RNA folding thermodynamics visualized by 2-aminopurine fluorescence. Biochemistry 2007;46:13948–60.
[70] Ballin JD, Prevas JP, Bharill S, Gryczynski I, Gryczynski Z, Wilson GM. Local RNA conformational dynamics revealed by 2-aminopurine solvent accessibility. Biochemistry 2008;47:7043–52.
[71] Gray RD, Petraccone L, Buscaglia R, Chaires JB. 2-Aminopurine as a probe for quadruplex loop structures. Methods Mol Biol 2010;608:121–36.
[72] Buscaglia R, Jameson DM, Chaires JB. G-Quadruplex structure and stability illuminated by 2-aminopurine phasor plots. Nucleic Acids Res 2012;40:4203–15.
[73] Unruh JR, Gokulrangan G, Lushington GH, Johnson CK, Wilson GS. Orientational dynamics and dye-DNA interactions in a dye-labeled DNA aptamer. Biophys J 2005;88:3455–65.
[74] Unruh JR, Gokulrangan G, Wilson GS, Johnson CK. Fluorescence properties of fluorescein, tetramethylrhodamine and Texas red linked to a DNA aptamer. Photochem Photobiol 2005;81:682–90.
[75] Espenson JH. Chemical kinetics and reaction mechanisms. New York, NY: McGraw-Hill; 1981.
[76] Bonnet G, Krichevsky O, Libchaber A. Kinetics of conformational fluctuations in DNA hairpin-loops. Proc Natl Acad Sci U S A 1998;95:8602–6.
[77] Wallace MI, Ying L, Balasubramanian S, Klenerman D. Non-Arrhenius kinetics for the loop closure of a DNA hairpin. Proc Natl Acad Sci U S A 2001;98:5584–9.
[78] Rhodes LM, Schimmel PR. Nanosecond relaxation processes in aqueous mononucleoside solutions. Biochemistry 1971;10:4426–33.
[79] Deng H, Braunlin WH. Kinetics of sodium ion binding to DNA quadruplexes. J Mol Biol 1996;255:476–83.
[80] Ida R, Wu G. Direct NMR detection of alkali metal ions bound to G-quadruplex DNA. J Am Chem Soc 2008;130:3590–602.
[81] Lane AN. The stability of intramolecular DNA G-quadruplexes compared with other macromolecules. Biochimie 2012;94:277–86.
[82] Green JJ, Ying L, Klenerman D, Balasubramanian S. Kinetics of unfolding the human telomeric DNA quadruplex using a PNA trap. J Am Chem Soc 2003;125:3763–7.
[83] Case DA, Simmerling CL, Wang J, Duke RE, Luo R, Walker RC, et al. AMBER12. San Francisco, CA: University of California; 2012.
[84] Le HT, Choudury I, Huang Y, Siow NC, Maguire JM, Trent JO. Quadgen. Louisville, KY: University of Louisville; 2013.
[85] Bergonzo C, Campbell AJ, Walker RC, Simmerling C. A partial nudged elastic band implementation for use with large or explicitly solvated large systems. Int J Quantum Chem 2009;109:3781–90.